NANO · MICRO small
www.small-journal.com

Magnetic Nanoparticles: A Review on Synthesis, Characterization, Functionalization, and Biomedical Applications

*Bahareh Rezaei, Parsa Yari, Sean M. Sanders, Haotong Wang, Vinit Kumar Chugh, Shuang Liang, Shahriar Mostufa, Kanglin Xu, Jian-Ping Wang, Jenifer Gómez-Pastora, and Kai Wu**

Nowadays, magnetic nanoparticles (MNPs) are applied in numerous fields, especially in biomedical applications. Since biofluidic samples and biological tissues are nonmagnetic, negligible background signals can interfere with the magnetic signals from MNPs in magnetic biosensing and imaging applications. In addition, the MNPs can be remotely controlled by magnetic fields, which make it possible for magnetic separation and targeted drug delivery. Furthermore, due to the unique dynamic magnetizations of MNPs when subjected to alternating magnetic fields, MNPs are also proposed as a key tool in cancer treatment, an example is magnetic hyperthermia therapy. Due to their distinct surface chemistry, good biocompatibility, and inducible magnetic moments, the material and morphological structure design of MNPs has attracted enormous interest from a variety of scientific domains. Herein, a thorough review of the chemical synthesis strategies of MNPs, the methodologies to modify the MNPs surface for better biocompatibility, the physicochemical characterization techniques for MNPs, as well as some representative applications of MNPs in disease diagnosis and treatment are provided. Further portions of the review go into the diagnostic and therapeutic uses of composite MNPs with core/shell structures as well as a deeper analysis of MNP properties to learn about potential biomedical applications.

1. Introduction

Magnetic nanoparticles (MNPs), with sizes below 1 µm (typically 1–100 nm), are a class of nanomaterials that can be manipulated by an external magnetic field. These nanoentities show very high surface-area-to-volume ratio and size-dependent physicochemical properties, making them particularly strong, versatile, and reactive compared to their bulk counterparts.[1] MNPs have been exploited in a wide range of applications due to their unique physical, chemical, and electrical properties, high surface area, strong mechanical and thermal stability, and high optical and magnetic characteristic.[2] Nowadays, they have been applied in areas such as data/energy storage,[3,4] spintronics,[5,6] catalysis,[7–9] magnetic inks,[10] environmental remediation,[11,12] gyroscopic devices,[13] and particularly, in the area of biomedicine.[14–16] The application of MNPs in the biomedical context is a fast-growing field, where MNPs are actively used as tracers in magnetic particle imaging (MPI) and magnetic particle spectroscopy (MPS)-based biosensors, contrast agents in magnetic resonance imaging (MRI) and nuclear magnetic resonance (NMR)-based biosensors, labels in magnetic biosensors, heating sources in hyperthermia therapy, carriers in drug and gene delivery, etc.[17,18]

To develop MNPs for biomedical applications, materials that exhibit high saturation magnetizations (Ms) are commonly selected. These include pure metals like Fe, Co, and Ni, alloys like FeCo, Alnico, and Permalloy, as well as ferrites like $MnFe_2O_4$, $CoFe_2O_4$, and $ZnFe_2O_4$.[19] Despite their high Ms, pure metals

B. Rezaei, P. Yari, S. Mostufa, K. Wu
Department of Electrical and Computer Engineering
Texas Tech University
Lubbock, TX 79409, USA
E-mail: kai.wu@ttu.edu
S. M. Sanders, H. Wang, J. Gómez-Pastora
Department of Chemical Engineering
Texas Tech University
Lubbock, TX 79409, USA
V. K. Chugh, J.-P. Wang
Department of Electrical and Computer Engineering
University of Minnesota
Lubbock, MN 55455, USA
S. Liang, J.-P. Wang
Department of Chemical Engineering and Materials Science
University of Minnesota
Lubbock, MN 55455, USA
K. Xu
Department of Computer Science
Texas Tech University
Lubbock, TX 79409, USA

The ORCID identification number(s) for the author(s) of this article can be found under https://doi.org/10.1002/smll.202304848

DOI: 10.1002/smll.202304848

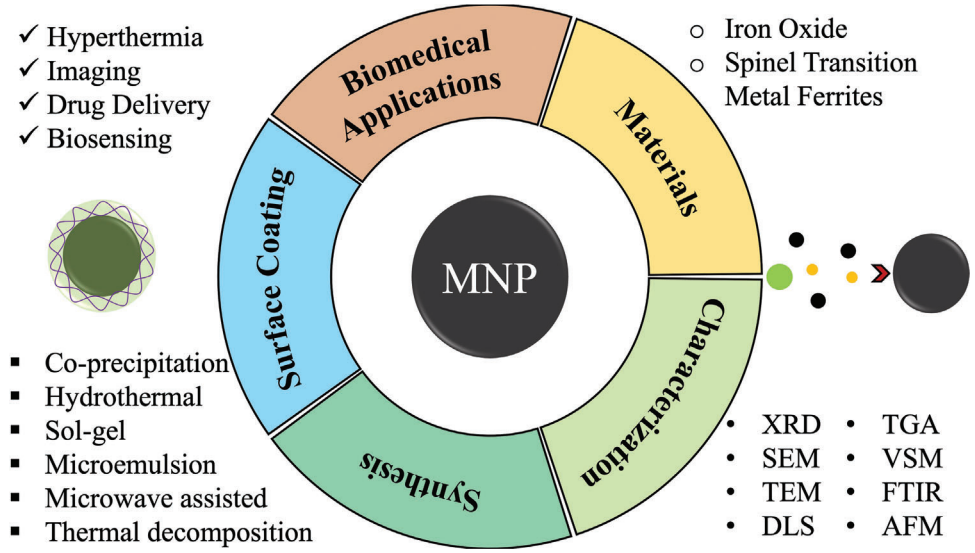

Figure 1. Topics covered in this review.

are not suitable for in vivo biomedical applications due to their high toxicity and oxidative properties. On the other hand, iron oxides (IO), such as Fe_3O_4 and γ-Fe_2O_3, have gained popularity for biomedical applications due to their excellent chemical and colloidal stability, as well as their high biocompatibility. As a result, IO MNPs are currently the most extensively researched materials for this purpose. Coating MNPs with ceramics, polymers, or highly charged/sterically hindered molecules can enhance their biocompatibility, suspension characteristics, and colloidal stability. Therefore, it is common practice to apply such coatings as a means of shielding MNPs. Encapsulating MNPs within a shell offers additional advantages, such as the ability to optimize functionalization and conjugation of proteins, enzymes, or antibodies, and the potential to create anticancer drug delivery systems. Since these characteristics can greatly affect their physical behavior, chemical properties, colloidal stability, and performance in biomedical applications, it is crucial to accurately and precisely monitor the synthesis details of MNPs and their successful surface functionalization.[1,14]

The production of MNPs can be broadly classified into two categories: "top-down", which involves reducing the size starting from the bulk material, and "bottom-up", which involves building up to the nanosized structures from molecular reagents.[17] These methods are also divided into three groups: i) condensation from vapor, ii) chemical synthesis, and iii) solid-state processes like milling. The methods described above offer the flexibility to synthesize pure, hybrid, and coated MNPs, depending on the specific requirements of the application, taking into account the suitability of hydrophilic or hydrophobic materials.[20] Chemical synthesis methods including coprecipitation, hydrothermal, sol–gel, microemulsion, thermal decomposition, and microwave-assisted approaches, are often preferred due to their ability to produce smaller MNPs with precise control over their size, shape, and uniformity (i.e., narrow size distribution).

As summarized in **Figure 1**, this review is structured as follows: in Section 2, we provide an overview of the different designs of MNPs, such as the material compositions, morphologies, and different characterization techniques. In Section 3, we review various chemical synthesis methods of MNPs, discussing the advantages and disadvantages of each method. In Section 4, we focus on the surface functionalization of MNPs, covering both inorganic and organic coatings. Section 5 presents various biomedical applications of MNPs, including magnetic hyperthermia therapy, MRI, drug delivery systems, biosensors, and MPI. Finally, we offer insights into the future trends of MNP structure design, as well as the potential for applying MNPs in novel biomedical applications.

2. Design of MNPs for Biomedical Applications

2.1. Materials for MNPs

In recent years, the field of nanotechnology has witnessed significant advancements in the synthesis of MNPs, resulting in the development of MNPs with precise and controlled morphologies and modified surfaces. These advancements have been made possible with the development of cutting-edge techniques and instrumentation, such as high-resolution microscopy and advanced spectroscopic techniques. With the ability to tailor the properties of MNPs to suit specific applications, researchers can now design and synthesize particles with enhanced functionality, biocompatibility, and stability. This level of control over the morphology and surface chemistry of MNPs has opened new avenues for their use in various fields, including biomedicine, environmental science, energy, and electronics. As a result, the potential applications of MNPs are rapidly expanding, and ongoing research in this field is expected to lead to further breakthroughs and innovations.

Spinel ferrite-based MNPs are metal oxides with a spinel structure, with the general formula AB_2O_4, where A and B are metallic cations located at two distinct crystallographic sites, namely, tetrahedral (the A site) and octahedral (the B site).[21,22] Among various spinel structures, transition metal ferrites MFe_2O_4 (M = Fe, Co,

Ni, Mn, Mg, Cu, Zn, etc.) have attracted increasing attention for biomedical applications, due to their high colloidal stability, biocompatibility, and ease of synthesis and functionalization.[23,24] Three different forms of spinel structures, including normal, inverse, and mixed, are known to exist based on the cation distributions at the two different sites. Tetrahedral and octahedral positions, respectively, are occupied in normal spinel by cations having oxidation values of 2^+ and 3^+. $ZnFe_2O_4$ is a form of normal spinel ferrite. In contrast to the 2^+ cations, which are entirely present at the octahedral sites, the 3^+ cations are evenly distributed at both sites in the inverse spinel. $NiFe_2O_4$ and Fe_3O_4 are the most typical types of inverse spinel ferrites. For instance, $MnFe_2O_4$ ($Mn_{0.8}Fe_{0.2}$ ($Mn_{0.2}Fe_{1.8}O_4$)) contains mixes of both oxidation states at both locations. Some of the more practical ferrite nanoparticles used in biomedical applications are discussed below.[21,24]

2.1.1. IO Nanoparticles

IO nanoparticles with the structural types of magnetite (Fe_3O_4) or maghemite (γ-Fe_2O_3) are the most widely used MNPs in biomedical applications due to the ease of synthesis, low cost, and high biocompatibility. Since Fe_3O_4 MNPs have a greater Ms, they are the preferred MNP in the field.[25] The size of the IO MNPs with an inverse spinel structure has a significant impact on its magnetic moment.[26] Bulk Fe_3O_4 exhibits ferromagnetic characteristics with a Curie temperature of 585 °C, and at a size below 20 nm, it becomes superparamagnetic.[21] In its reverse structure, Fe^{3+} cations occupy the A sites, while an equal amount of Fe^{2+} and Fe^{3+} cations occupy the B sites.[26] The use of Fe_3O_4 MNPs is crucial in a variety of medical procedures, including MRI, magnetically guided medication administration, and hyperthermic cancer treatment. It is one of the several biocompatible superparamagnetic nanoparticles that have been thoroughly explored and used.[27]

2.1.2. Spinel Transition Metal Ferrites MFe_2O_4 (M = Mn, Zn, Ni, Co)

One of the most prevalent spinel ferrites with neither an inverse nor a normal structure is manganese ferrite. It belongs to a class of soft magnets called mixed spinel magnets, where Mn^{2+} cations partially occupy both the A and B sites.[21] Its Curie temperature in bulk is between 550 and 620 °C.[28] For the same particle size, it has lower magnetic anisotropy, and higher Ms and magnetic permeability than Fe_3O_4. This material has drawn particular interest among spinel ferrites in the biomedical field as a drug delivery system and MRI contrast agent.[29] Furthermore, it can also be used as the core or shell components in materials for hyperthermia treatment to increase the effectiveness of the cancer treatment.[30]

Zinc ferrite has a typical spinel structure with Zn^{2+} and Fe^{3+} cations located in the tetrahedral and octahedral sites, respectively. It exhibits paramagnetic characteristics in bulk form and ferromagnetic characteristics in nanosized structures because of the partial migration of Zn^{2+} cations to the octahedral site. Like other ferrites, the synthesis technique and particle size have a great influence on the application, as these affect the electrical, and magnetic properties of this material. It also has a wide range of applications in the biomedical areas.[28,29]

The well-known soft magnet nickel ferrite has an inverted spinel structure, with Fe^{3+} evenly distributed across tetrahedral and octahedral sites and Ni^{2+} situated at the octahedral site. In many biomedical applications, the $NiFe_2O_4$ MNPs are used as the core material. $NiFe_2O_4$ MNPs, like the other ferrites discussed before, are crucial for MRI applications because of their cost-effectiveness, great electromagnetic properties, moderate Ms, and good chemical stability.[21,28] Quantitative cytotoxicity tests of both coated and uncoated $NiFe_2O_4$ MNPs at various pH levels demonstrated that neither kind of MNP is cytotoxic, indicating that $NiFe_2O_4$ MNPs can be widely used for hyperthermia cancer treatment.[31]

Cobalt ferrite ($CoFe_2O_4$) is an inverse spinel ferrite where all the Co^{2+} cations and the remaining half of the Fe^{3+} cations occupy the octahedral sites. The high magnetocrystalline anisotropy of Co^{2+} cations in octahedral cavities causes the high anisotropy of $CoFe_2O_4$. Cobalt ferrite MNPs are of relevance in the biomedical fields due to their high magnetocrystalline anisotropy, high coercivity at ambient temperature, and good Ms. The superparamagnetic behavior is also seen to grow with decreasing particle size for $CoFe_2O_4$ MNPs smaller than 10 nm.[32,33]

2.2. MNP Morphology

Scientists have now been successful in creating a useful hybrid class of MNPs called core/shell MNPs (also noted as core–shell MNP and core@shell MNPs), which can be defined as well-organized nanomaterials consisting of two or more types of nanocomponents.[34] In general, MNPs are comprised of a single element, while composite and core/shell MNPs, as the name suggests, are composed of two or more materials. These include a variety of closely related combinations such as inorganic/inorganic, inorganic/organic, organic/inorganic, and organic/organic materials.[20,35] The choice of shell material for a core/shell MNP is highly dependent on the intended application. The synthesis of core/shell MNPs provides the opportunity to use a diverse range of materials as core and shell, enabling the customization of unique features and functionalities. The physicochemical, biological, optical, and other properties of the core/shell MNPs can be modified by altering the building blocks comprising the core and/or shell layers. This allows the synthesis of a wide range of core/shell MNPs, each with unique properties and functions, making them useful for numerous applications for a variety of fields such as medicine, pharmacy, engineering, and material science.[36] It has been found that the addition of a shell layer can significantly modify the properties of the original core. In fact, the shell can impart new synthetic or catalytic reactivity to the core. Furthermore, the thermal stability and dispersibility of the core can be improved through shell addition. Additionally, novel optical and electronic properties can be induced in the core nanoparticle through the formation of a core/shell structure. Therefore, these modified structures can offer combined functionalities of both the core and the shell with unique properties beyond those of the individual components alone.[37]

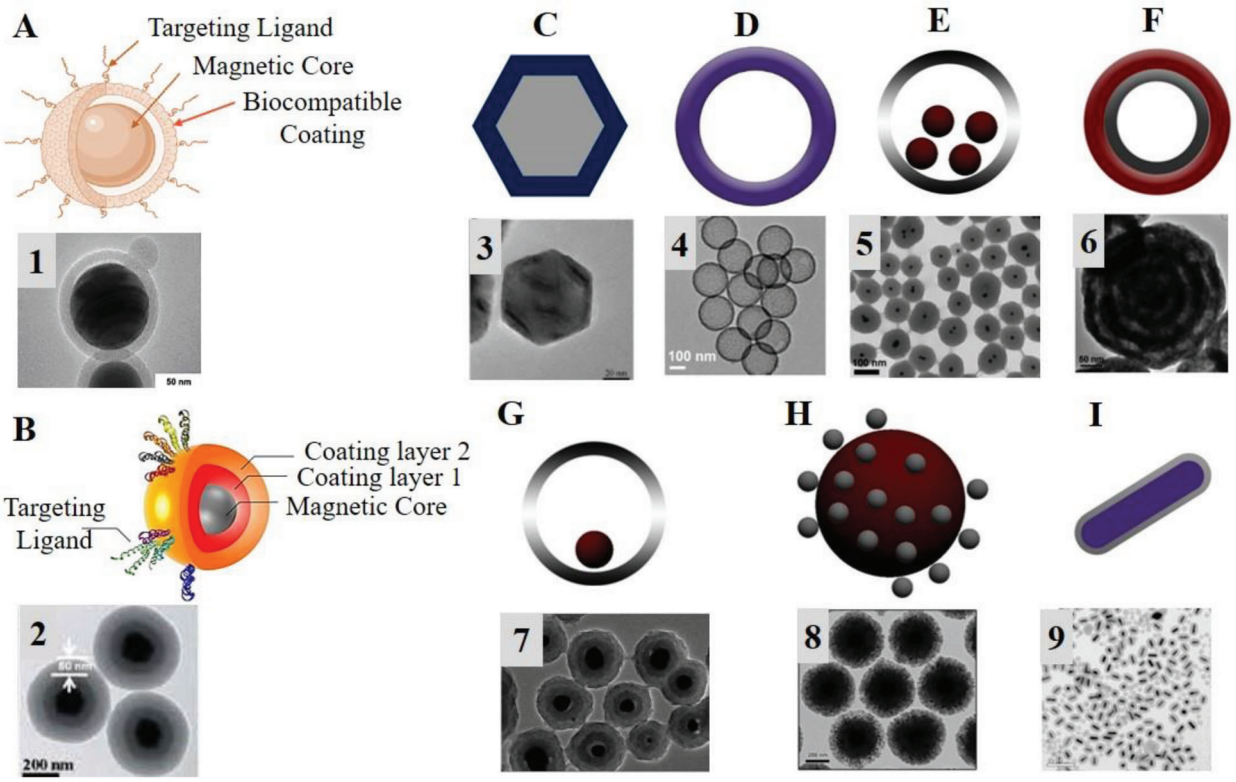

Figure 2. Schematic view of MNP structures and corresponding transmission electron microscopy (TEM) images. A, 1) Core/shell nanoparticles. B, 2) Core/shell/shell nanoparticles, also called core/multishell nanoparticles. C, 3) Polyhedral core/shell nanoparticles. D, 4) Hollow core/shell nanoparticles, also called single shell nanoparticles. E, 5) Moveable multicore/shell nanoparticles. F, 6) Hollow core/shell/shell nanoparticles. G, 7) Moveable core/shell nanoparticles. H, 8) Core/porous shell nanoparticles. I, 9) Rod core/shell nanoparticles. A, 1) Reproduced under the terms of the CC BY 2.0 license.[39] Copyright 2015, IOP Science. B, 2) Reproduced with permission.[40] Copyright 2013, The Royal Society of Chemistry. C, 3) Reproduced with permission.[41] Copyright 2016, The Royal Society of Chemistry. D, 4) Reproduced under the terms of the CC BY 4.0 license.[42] Copyright 2019, MDPI. E, 5) Reproduced with permission.[43] Copyright 2014, Elsevier Ltd and Techna Group S.r.l. F, 6) Reproduced with permission.[44] Copyright 2007, Wiley-VCH GmbH & Co. KGaA, Weinheim. G, 7) Reproduced with permission.[45] Copyright 2011, The Royal Society of Chemistry. H, 8) Reproduced with permission.[46] Copyright 2008, Wiley-VCH GmbH & Co. KGaA, Weinheim. (I, 9) Reproduced under the terms of CC BY 4.0 license.[47] Copyright 2016, Frontiers.

To date, numerous MNPs structures have been described, including the core/shell structure such as most single- and multicore nanoparticles (see **Figure 2**A, 1), the core/double shell nanoparticles or core/multishell nanoparticles (see Figure 2B, 2), the polyhedral core/shell nanoparticles (see Figure 2C, 3), the hollow core/shell nanoparticles with single or multiple shells nanoparticles (see Figure 2D, 4 and F, 6), moveable core/shell nanoparticles with single or multiple cores (see Figure 2E, 5 and G, 7), core/porous shell nanoparticles (see Figure 2H, 8), and rod core/shell nanoparticles (see Figure 2I, 9).[36,38]

The characteristics of MNPs are inherently influenced by both their geometric attributes and dimensions. Notably, attributes such as the blocking temperature, saturation magnetization, and magnetic permeability exhibit variations in response to alterations in particle size. Consequently, meticulous control over crystal dimensions and morphology assumes paramount significance in the determination of the chemical and physical attributes of MNPs, as underscored in existing literature.[20,48] A distinctive magnetic phase termed superparamagnetism manifests in diminutive ferrimagnetic or ferromagnetic nanoparticles. This phenomenon occurs within a size spectrum spanning from a few nanometers to fractions of a nanometer, contingent on the specific material properties. In this regime, the cumulative magnetic moment of the nanoparticle, a result of the amalgamation of individual atomic magnetic moments, collectively assumes a colossal magnetic orientation. For example, in MNPs with modest dimensions and possessing uniaxial anisotropy, their magnetic moments are susceptible to stochastic alterations driven by thermal fluctuations, a phenomenon inherently linked to temperature variations. This susceptibility stems from the diminution of the anisotropic barrier energy (ΔE) below a critical size, rendering it vulnerable to the prevailing thermal energy denoted as $k_B T$, where k_B signifies the Boltzmann constant and T denotes temperature. The determination of the critical size, signifying the transition from superparamagnetism to single- to multidomain structural configurations, conventionally rests upon the examination of coercivity (H_c) and remanent magnetization concerning particle size. However, this critical size for Fe_3O_4 MNPs remains contingent upon the underlying crystal structure, which may encompass spherical, cubic, or diverse phases, thus contributing to its as-yet unestablished nature. Consequently, a comprehensive assessment of the critical size in congruence with the crystal structure is imperative. Theoretical estimations posit a requisite size of 76 nm for cubic and 128 nm for

spherical Fe_3O_4 MNPs to attain a multidomain configuration.[48] Nevertheless, the attainment of superparamagnetism in Fe_3O_4 MNPs is generally surmised to necessitate dimensions below 15 nm, in accordance with predictions formulated by Frenkel and Dorfman.[19,49] This delineation underscores the intricate interplay between nanoparticle dimensions, crystal structure, and thermal effects in elucidating the magnetic attributes of these nanoparticles.

Also, due to the strong surface anisotropy effect, the effective magnetic anisotropy (or magnetic coercivity) of the MNPs is solely reliant on the particle shape. In addition, the particle shape also plays a significant role in determining the physical and chemical characteristics of the material, including its melting point, electrical and optical properties, catalytic activity, and selectivity.[20]

In relation to their magnetic properties, magnetic core/shell nanostructures possess remarkable qualities. They can be sorted using external magnets, which is an advantage over traditional filtration and centrifugation methods. For this reason, magnetic core/shell nanoparticles have been proposed as a promising material in magnetic separation.[50] Core/shell nanoparticles consist of a central magnetic core enveloped by an outer shell with distinct properties, often of different materials. The interaction between the core and shell gives rise to exchange coupling, which is the transfer of magnetic moments between these regions. This coupling can have a significant impact on the overall magnetic behavior of the nanoparticle. The exchange interaction arises due to the overlap of electron wave functions between neighboring atoms in a material. In the context of core/shell nanoparticles, this interaction occurs across the interface between the core and the shell, leading to a transfer of magnetic moments and alignment of spins. The strength and nature of the exchange coupling depend on various factors, including the materials used for the core and shell, their crystal structures, lattice constants, and the thickness of the shell. There are two main types of exchange coupling that can occur in core/shell nanoparticles: 1) direct exchange coupling and 2) indirect exchange coupling. The exchange coupling in core/shell-structured magnetic nanoparticles is a complex phenomenon and, in this review, we will not elaborate on this topic. This coupling significantly influences the nanoparticles' magnetic properties and can be tailored for specific applications across various domains, including medicine, data storage, and nanotechnology.

Herein, this review focuses on the applications of single- and multicore MNPs, which are subordinate to core/shell and core/multishell structures. The magnetic moment of a single-core MNP originates from the magnetic core when using diamagnetic shells, so in addition to selecting MNPs with high Ms, using larger magnetic cores is another option to generate higher torque single-core MNPs, making core/shell MNPs more suitable for certain applications in biomedical fields.[38]

2.3. Characterization Techniques for MNPs

To investigate the size distribution, shape, surface charge, and porosity of nanoparticles in various environments, numerous MNP characterization techniques have been developed. Here, we discuss some widely used methods for characterizing the physicochemical properties of MNPs in both dry and solution states. We also cover some advanced methods for characterizing MNPs that broaden the scope of information that may be accessed and provide a better understanding of the nanoparticle characteristics.

2.3.1. Magnetometry

Vibration Sample Magnetometer (VSM): VSM is a sophisticated approach for quantifying the magnetic moment of materials based on the interaction of magnetic forces. As illustrated in **Figure 3**A, the VSM system embodies a comprehensive methodology wherein the magnetic properties of a sample are discerned through the meticulous measurement of voltage alterations arising from its perpendicular vibration within an externally applied magnetic field. This technique stands as a cornerstone for providing precise and intricate insights into a material's magnetic moment, elucidating how it evolves concerning distinct variables such as temperature, magnetic field intensity, and crystal orientation.[51] Upon introducing the specimen into a consistent magnetic field, a process commences where magnetic domains or individual magnetic spins harmonize their alignment with the applied field. Consequently, the material undergoes magnetization, transforming its inherent magnetic state. The operational foundation of the VSM technique is established upon the Lenz–Faraday magnetic induction law, an empirical principle that asserts that variations in magnetic flux can induce voltage in detection coils. These coils are strategically positioned to encapsulate the magnetic field flux, and the consequential voltage fluctuations are meticulously measured. This dynamic interplay between magnetic flux and induced voltage is at the core of the VSMs functional mechanism.

A central facet of the VSM technique lies in its ability to capture magnetization curves, commonly known as hysteresis loops (or M–H curves), at ambient temperatures through the integration of control and monitoring software.[52] These hysteresis curves offer a visual depiction of the intricate relationship between the applied magnetic field and the resultant magnetization of the material. The curves delineate essential magnetic characteristics such as magnetization remanence, coercivity, and saturation magnetization.[53] By closely analyzing these attributes, researchers can gain profound insights into the material's magnetic behavior, shedding light on its domain structure, magnetic anisotropy, and overall magnetic stability.

Superconducting Quantum Interference Device (SQUID): SQUID is a remarkable advancement in the field of magnetometry, enabling the precise determination of the magnetic properties of nanoparticles at an unprecedented level of sensitivity.[54] With its extraordinary capability to detect magnetic fields as weak as 10^{-18} T, the SQUID technique has revolutionized the way researchers study and characterize nanoparticles' magnetic behavior.

At the heart of the SQUID technique lies a superconducting loop that exhibits quantum interference effects. This loop is usually constructed using superconducting materials, which can conduct electric current without resistance when cooled to very low temperatures. The SQUID magnetometer operates based on

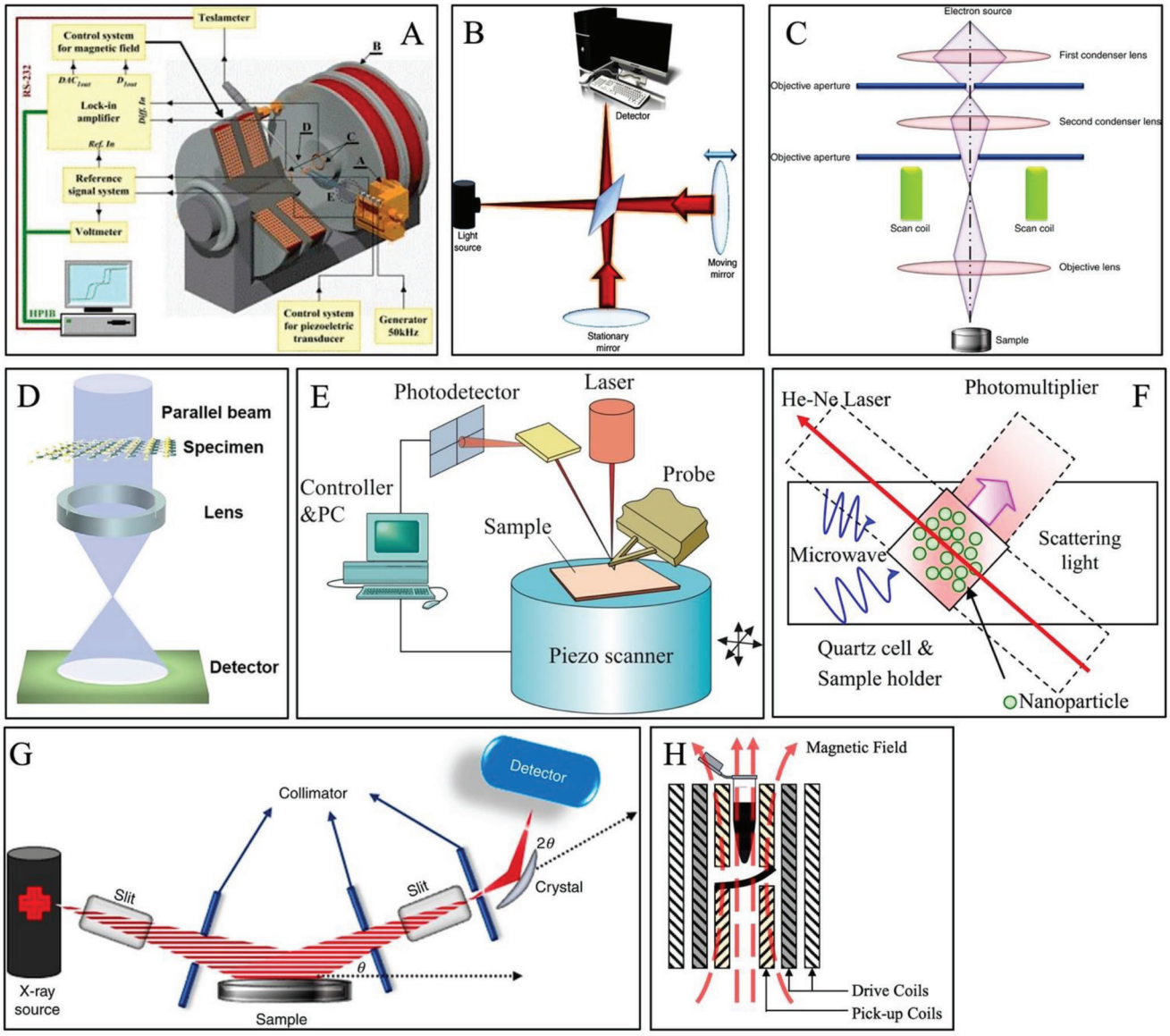

Figure 3. A–H) Working principle of each characterization technique: A) VSM, B) FTIR, C) SEM, D) TEM, E) AFM, F) DLS, G) XRD, and H) MPS. A) Reproduced under the terms of CC BY 3.0 license.[77] Copyright 2018, IOP Science. B,C,G) Reproduced with permission.[78] Copyright 2017, Elsevier Inc. D) Reproduced with permission.[79] Copyright 2021, Elsevier Inc. E) Reproduced under the terms of CC BY 4.0 license.[80] Copyright 2019, Parabole. F) Reproduced with permission.[81] Copyright 2015, Springer Nature.

the Josephson effect, where pairs of Cooper electrons, formed due to superconductivity, can tunnel across a thin insulating barrier. This phenomenon gives rise to remarkable sensitivity to magnetic flux changes, allowing the SQUID to detect even the tiniest magnetic signals emanating from nanoparticles.

One of the key attributes of the SQUID technique is its ability to precisely quantify the magnetic moment of individual MNPs. This characteristic is invaluable for investigating the magnetic behavior of nanoscale materials, including but not limited to blocking temperature, magnetization remanence, and saturation magnetization.[55,56] The technique's sensitivity extends to nanoparticle ensembles as well, making it an essential tool for probing collective magnetic phenomena in materials.

2.3.2. X-Ray Diffraction (XRD)

XRD is an excellent nondestructive method for the characterization of both organic and inorganic crystalline materials at the atomic level. This technology can be used to examine crystal and molecular structures, identify various compounds qualitatively, quantitatively resolve chemical species, assess the degree of crystallinity, detect isomorphous substitutions, and determine phase characteristics.[54] Additionally, XRD can measure particle sizes and provide other valuable information.[57] In order to obtain this information, the full width at half maximum (FWHM) of the Bragg reflections needs to be analyzed.[54,58] As shown in Figure 3G, the diffraction patterns are obtained when an X-ray

bounces off a crystal, and these patterns reveal the crystal formations. Although XRD offers several advantages, it is not without limitations. One drawback is the challenge of obtaining well-formed crystals, which can hinder the accuracy and reliability of the results. Additionally, the scope of information that can be obtained from XRD is somewhat limited.[57]

The Scherrer equation (Equation (1)) is used to estimate the mean crystal size along a specified crystallographic direction. This equation assumes an ideal scenario where a monochromatic, infinitely narrow, and perfectly parallel X-ray beam is incident on a monodisperse powder composed of cube-shaped crystallites. The equation is expressed as

$$D_{hkl} = \kappa\lambda / B_{hkl} \cos\theta \quad (1)$$

where *hkl* are the Miller indices of the planes that belong to the peak that is being studied, κ is a numerical factor commonly referred to as the crystallite-shape factor, λ is the X-ray wavelength, B_{hkl} is the FWHM of the diffraction peak in radians, and θ is the Bragg angle. D_{hkl} is the crystallite size along the direction perpendicular to the lattice planes.[58]

2.3.3. Transmission Electron Microscopy (TEM)

TEM, as shown in Figure 3D, uses an electron beam to interact with an ultrathin sample, offering highly precise and high-resolution imaging information on the size, shape, morphology, state of aggregation, and distribution of nanoparticles at the nanometer scale.[58–60] The preparation of the ultrathin sample takes time, skill, and a high level of vacuum, and results are more reliable for homogeneous samples. Moreover, high-resolution TEM (HRTEM) is a phase-contrast TEM mode that offers the best resolution and aids in visualizing atomic packing (atomic lattice) in nanoparticles, providing a picture of the crystal defects.[57,59] To determine the size distribution, the individual size of ≈1000 randomly chosen nanoparticles should be measured after a representative set of photographs of the sample has been collected. The process can be carried out manually or automatically utilizing particle analysis techniques.[58]

2.3.4. Scanning Electron Microscopy (SEM)

SEM is a surface imaging method for electron microscopy that is capable of fully resolving a range of particle sizes, size distributions, nanomaterial forms, and surface morphology of synthesized particles at the micro- and nanoscales.[60] By manually measuring and counting the particles or by utilizing specialized software, we can use SEM to investigate the morphology of the particles and build a histogram from the images.[57] A fundamental requirement for SEM to work in vacuum is to avoid the interaction of electrons with gas molecules in order to achieve high resolution. As shown in Figure 3C, the SEM instrument is based on the theory that primary electrons released from the source provide energy to the sample atomic electrons, which can then be released as secondary electrons (SE). An image can be formed by collecting these SE from any point of the sample.[61]

2.3.5. Dynamic Light Scattering (DLS)

DLS can examine the size distribution of small particles in solution or suspension on a scale ranging from 1 nm to several micrometers. This technique primarily depends on Rayleigh scattering from the suspended nanoparticles to quantify the light scattered from a laser as it passes through a colloid.[57] DLS is also one of the most used techniques for measuring the size distribution of MNPs in suspension. As shown in Figure 3F, the MNP suspension is exposed to an electromagnetic wave during the DLS measurement, and as the electromagnetic wave impinges on the MNP, scattering causes the electromagnetic wave's direction and strength to change. Since the MNPs' kinetic energy causes them to move randomly, the variation of intensity over time provides information about this motion and may be used to calculate the particles' diffusion coefficient.[62] However, due to a few unrecognized effects, including the concentration of the particle suspension, the scattering angle, and the shape anisotropy of the nanoparticles, the accuracy of the determined particle size is not fully known.

2.3.6. Atomic Force Microscopy (AFM)

In AFM, a finely pointed probe undergoes a systematic raster scan across the surface of the sample with a remarkable positioning accuracy at the sub-nanometer level. Throughout the scanning process, a feedback loop ensures that the probe maintains a consistent interaction with the sample by modulating its vertical movements. The recorded vertical movements are then correlated with the *XY* position, ultimately resulting in a detailed surface topography of the sample[63] as shown in Figure 3E.

Three different scanning modes are available for AFM, including contact mode, noncontact mode, and intermittent sample contact mode to study the dispersion and aggregation of nanomaterials as well as their size, shape, sorption, and structure. AFM can also be used to characterize in real-time how supported lipid bilayers interact with nanomaterials, something that is currently not possible to do with current electron microscopy methods. AFM can measure up to the sub-nanometer scale in aqueous fluids and does not require oxide-free, electrically conductive surfaces for the measurement. Moreover, it does not significantly harm many different native surface types. However, a significant flaw is the cantilever's size, which causes an overestimation of the samples' lateral dimensions.[57,64]

2.3.7. Fourier Transform Infrared (FTIR) Spectroscopy

As shown in Figure 3B, FTIR uses infrared light to scan the samples and identify organic, inorganic, and polymeric components. Changes in the material composition are reflected in the pattern of absorption bands, allowing for the identification and characterization of unknown components, detection of additives, identification of decomposition, and characterization of oxidation and contamination.[65] In academic and industrial research, FTIR spectroscopy is frequently employed to determine if biomolecules are successfully attached to the surface of nanoparticles. The study of nanoscale materials has also

been expanded by FTIR, including the confirmation of functional molecules covalently grafted onto MNPs, carbon nanotubes, graphene, and gold nanoparticles, as well as interactions between enzymes and substrates throughout the catalytic process.[57,59]

2.3.8. Thermogravimetric Analysis (TGA)

TGA is an experimental method for determining how much a sample's mass changes as a function of temperature and/or time in a controlled environment.[66] The analyzer consists of a furnace with a temperature programmer and controller, a sample pan, and an exact microbalance attached to it.[66] TGA can be used to identify a sample's residual metal concentration, absorbed moisture content, polymer properties and features, and polymer decomposition temperatures. The amount of coating on a nanoparticle's surface can also be determined via TGA.[67]

2.3.9. Magnetic Particle Spectroscopy

MPS records the dynamic magnetization response of MNPs under the application of AC drive fields which may constitute a single-frequency or a dual-frequency excitation field. A schematic depiction of a dual-frequency MPS system has been shown in Figure 3H. The MPS system consists of drive coils for the generation of the AC drive field and a balanced set of pick-up coils for recording the magnetization response of MNPs. Under application of the excitation field, the MNPs undergo both the Néel and Brownian relaxation processes, which are determined by not only the MNP physical parameters such as core size and saturation magnetization of the materials, but also by the physical properties of the surrounding media. Thus, the recorded magnetization response can be used for the characterization of the temperature[68] and viscosity[69] of the surrounding media, and also as a unique magnetic signature of the MNPs for magnetic colorization applications.[70]

2.3.10. AC Susceptometry (ACS)

The experimental setup for ACS measurements is similar to that of single-frequency MPS measurements. In both cases, a single-frequency drive field is used to magnetically excite a sample of MNPs, and the magnetization response is recorded using a balanced set of pick-up coils. The main difference between ACS and MPS is the magnitude of the applied excitation field. MPS uses a large excitation field to drive the MNPs into their nonlinear response regime. ACS, on the other hand, uses a smaller excitation field (around one order of magnitude smaller) to record the changes in the slope of the M–H response curve. The AC magnetization response captured in ACS measurements yields two quantities: the susceptibility (χ) and the phase lag (ϕ) to the applied magnetic field. ACS measurements can be performed using either custom-built systems[71–73] or commercial systems such as the DynoMag system from Acreo.[74] The ACS systems have been successfully reported for applications including the determination of MNP core and hydrodynamic size distributions[72,75] to bioassay applications utilizing clustering of MNPs.[76]

3. Chemical Synthesis of MNPs

3.1. Coprecipitation

Coprecipitation, which involves adding a base as a precipitating agent at either room temperature or a higher temperature, is an easy and practical method for synthesizing MNPs from aqueous salt solutions. The precipitation process offers a significant advantage in the production of a large amount of MNPs.[82–84] The method's simplicity, its high yield, and promise for less time-intensive and readily scalable industrial application make coprecipitation one of the most preferred synthesis method.[85–87] For instance, by hydrolyzing an aqueous solution comprising of a base and iron salts at room temperature in an open environment, Fe_3O_4 MNPs can be synthesized. Fe^{2+} and Fe^{3+} can be coprecipitated to produce magnetite (Fe_3O_4) MNPs as described by the following chemical reaction[85,88,89]

$$Fe^{2+}(aq) + 2Fe^{3+}(aq) + 8OH^- \rightarrow Fe_3O_4(s) + 4H_2O \quad (2)$$

Aqueous solutions of Fe^{3+} and M^{2+} salts, where M^{2+} is a d-block transition metal, are often combined with a base solution to prepare metal ferrite MNPs. Since only kinetic factors are involved in the formation of crystals, the control over particle size distribution is limited. In addition, this approach still has some disadvantages, such as the inability to control particle shape, crystallinity, and magnetic characteristics.[82] In order to fine-tune the size, shape, and chemical makeup of the obtained MNPs, it is crucial to control the reaction parameters such as the type of metal cation precursors, the molar ratio between the M^{2+} and Fe^{3+} cations, reaction temperature, pH value, as well as the type and concentration of the alkaline agent.[82,90] The chemical reaction that occurs can be described as follows[91]

$$M^{2+}(aq) + 2Fe^{3+}(aq) + 8OH^-(aq) \rightarrow MFe_2O_4(s) + 4H_2O(aq) \quad (3)$$

Multiple groups have used this method for producing magnetic nanosized materials. For example, Darwish et al. used a controlled coprecipitation to produce ferrite MNPs, including cobalt ferrite (CF-MNPs) and zinc cobalt ferrite (ZCF-MNPs) particles, as reported in their study.[92] The synthesis procedure employed by these authors is a simplified, environmentally friendly, and low-temperature process that can be carried out in air, with a maximum ambient temperature of 60 °C. Their method does not require any oxidizing or coating agents and it is a modified version of the conventional coprecipitation method, with alternations made to the precursor material's composition, specifically the molar ratio of the cations, Fe^{3+}:Fe^{2+}:Co^{2+}/Zn^{2+}, which is set to 3:2:1.

Figure 4A illustrates the TEM image of the CF-MNPs, which have an average particle size of 8 ± 2 nm. The average particle size of ZCF-MNPs is 25 ± 5 nm with a wide size distribution and visible agglomeration behavior (see Figure 4D). HRTEM was used to observe the crystalline nature of the synthesized MNPs. The evident lattice border in the HRTEM image shows that the CF-MNPs have a higher crystallinity than

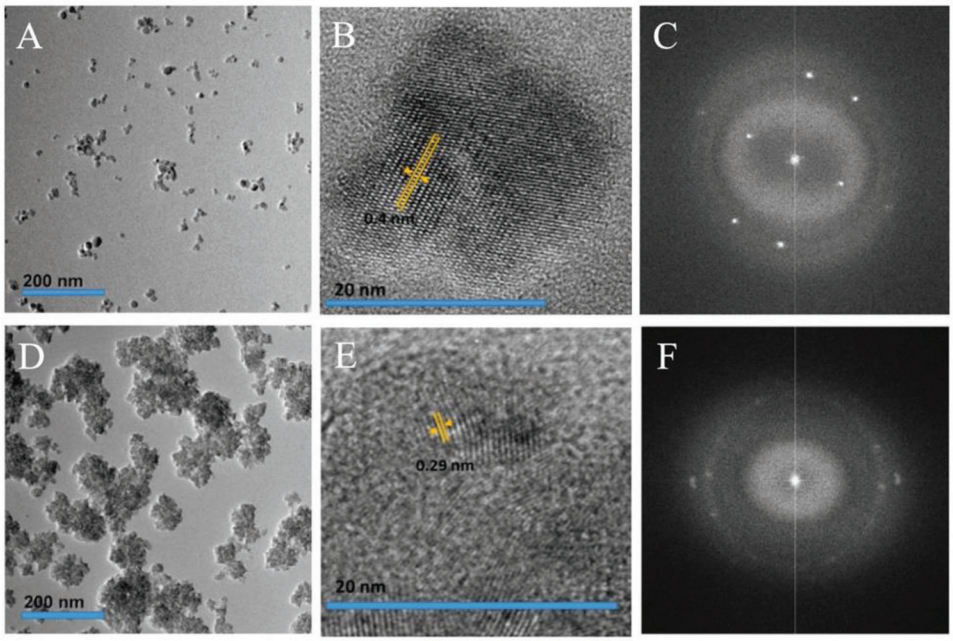

Figure 4. TEM, HRTEM, and SAED of A–C) CF-MNPs and D–F) ZCF-MNPs, respectively. Reproduced under the terms of the CC BY 4.0 license.[92] Copyright 2019, MDPI.

the ZCF-MNPs (see Figure 4B,E). The related selected area electron diffraction (SAED) image of the MNPs (see Figure 4C,F) shows the ring properties typical of a structure made up of small domains with their crystallographic axes aligned at random directions. The SAED pattern exhibits diffuse rings with reduced intensity that are linked to the plane reflections of the MNPs. Results show that, compared to the ZCF-MNPs, the reported method produced smaller nanoparticles with fewer aggregations for the CF-MNPs. In addition, the produced MNPs (both ZCF-MNPs and CF-MNPs) displayed an Ms of 50 emu g^{-1}, a moderate level of optical activity, and a great specific loss power (SLP) characteristic compared to commercial IO materials under the same magnetic field strength (40 kA m^{-1}). Because of the high SLP, the nanoparticles made with the suggested approach show promise for hyperthermia treatment of cancer.

In another study reported by Shen et al., a convenient coprecipitation technique was used to successfully produce shape-controlled magnetite nanoparticles.[93] The TEM images in **Figure 5**A show that the morphology of the magnetite nanoparticles changed from nanospheres to nanoneedles and then to nanocubes as the amount of sodium dodecyl sulfate was adjusted during reaction. XRD patterns in Figure 5B indicate that all the reported shapes were of the pure Fe_3O_4 phase. Figure 5C illustrates the appealing magnetic characteristics and high Ms of the Fe_3O_4 MNPs, as evidenced by their magnetic hysteresis loops.

3.2. Hydrothermal Method

Hydrothermal synthesis utilizes various wet-chemical processes to create MNPs. The hydrothermal method is based on heating and dissolving iron precursors in an aqueous media at high temperatures and elevated pressure. In a Teflon-sealed stainless-steel autoclave with supercritical/sub-supercritical water, chemical processes are accrued. The ultimate IO phase is formed by dehydrating the hydroxide intermediates ($Fe(OH)_n$) produced during the hydrolysis of ferrous ions.[85] Several factors can dramatically influence the reaction kinetics and nucleation rate in this method, including the synthesis temperature and precursor concentration.[94] For example, the precursor concentration could lead to an increased particle size and a wider size distribution. The average particle size is more dependent on the reaction time than on the precursor concentration, although there is an impact.[95,96]

A schematic representation of the hydrothermal approach is shown in **Figure 6**. This synthesis method allows for excellent control of the MNP composition and avoids the formation of dislocations in single-crystal MNPs. This is achieved by utilizing either aqueous or nonaqueous solutions. This process is particularly useful for producing hollow MNPs with precise shapes, such as nanotubes and nanorings.[94] This method utilizes low-cost raw materials and can achieve excellent control over the morphology of the resulting nanoparticle.[85]

Several authors have used this approach for synthesizing MNPs with excellent properties. Peng et al. studied the hydrothermal synthesis and magnetic properties of gadolinium-doped cobalt ferrite nanoparticles.[97] In their work, $CoFe_{2-x}Gd_xO_4$ (x = 0–0.25) MNPs were synthesized via a simple hydrothermal process at 200 °C for 16 h without the assistance of surfactants. At a dopant level of $x \leq 0.25$, the XRD data demonstrated that the synthesized powders were pure phase, and the peaks could be easily indexed to the cubic spinel cobalt ferrite (see **Figure 7**C). The gadolinium-doped cobalt ferrite nanoparticles were single crystals, generally spherical, uniformly dispersed, and not

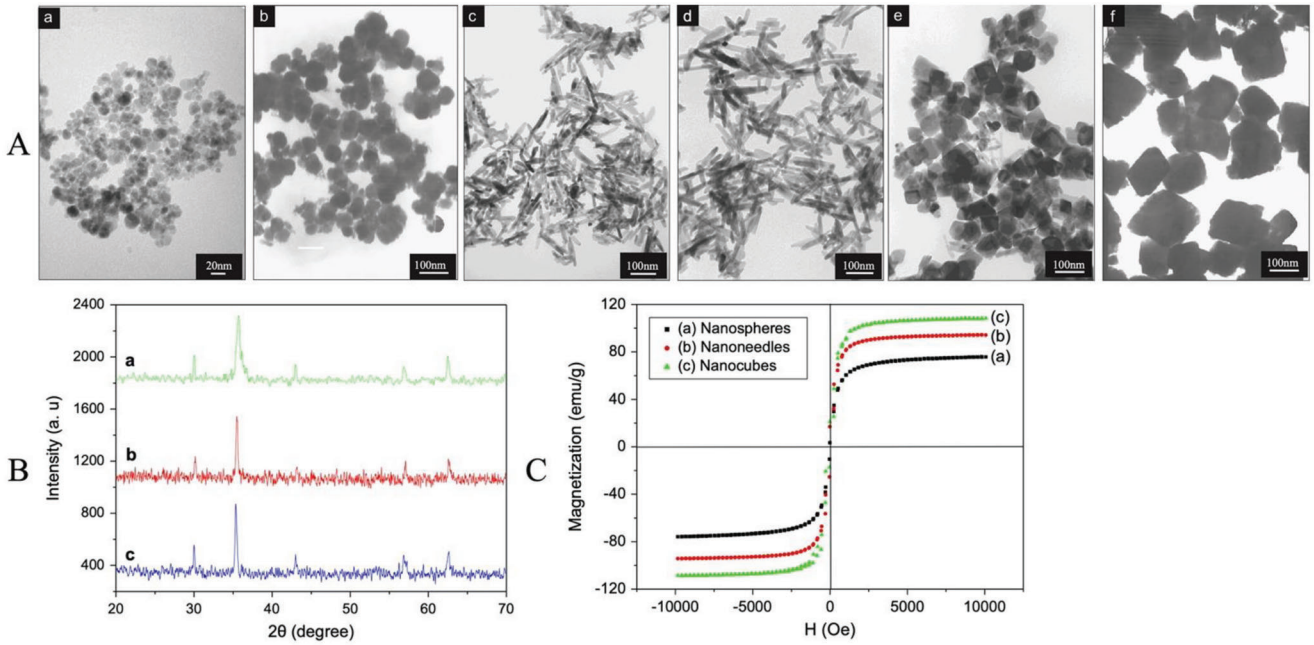

Figure 5. A) TEM images of magnetite nanoparticles. B) XRD, and C) magnetic hysteresis loops of (a) nanospheres, (b) nanoneedles, and (c) nanocubes. Reproduced with permission.[93] Copyright 2013, Elsevier Ltd and Techna Group S.r.l.

significantly agglomerated, according to the TEM and HRTEM observations in Figure 7A,B. The rare-earth element doping had a significant impact on the Ms and coercivity due to significant lattice distortion and small particle grain development, according to the measurements of the magnetic hysteresis loop (M–H curves) at ambient temperature.

In another study, an in situ hydrothermal method was used to successfully produce a magnetic hydroxyapatite nanocomposite designated as IO–HA.[98] The nanorod shape of the IO–HA was confirmed by the TEM investigation (see **Figure 8**A). As it is obvious from the XRD pattern (Figure 8B), the IO–HA nanocomposite did not contain any impurity phases. A prolonged release of a loaded compound (curcumin) from the nanocomposite indicated that a good and maximal release was achieved due to the degradation of the HA component of the nanocomposite in an acidic environment. An in vitro MRI study supported the fact that IO–HA had a sufficient superparamagnetic property, which makes it advantageous for imaging applications (see Figure 8C). Moreover, the IO–HA nanocomposite showed great biocompatibility since it had no cytotoxic or hemolytic effects. As a result, the IO–HA nanocomposite is proposed as a theragnostic T2-MRI contrast agent.

3.3. Sol–Gel

The sol–gel process involves the hydroxylation and condensation of molecular precursors in a solution to form a "sol" composed of nanoparticles. Once the solvent is removed or a chemical reaction occurs, the "sol" is dried or "gelled" to form a 3D metal oxide network. The properties of the gel are strongly influenced by the structure of the sol phase during the sol-gel process, which determines the gel's shape, size, and porosity. Furthermore, several factors influence the kinetics, growth processes,

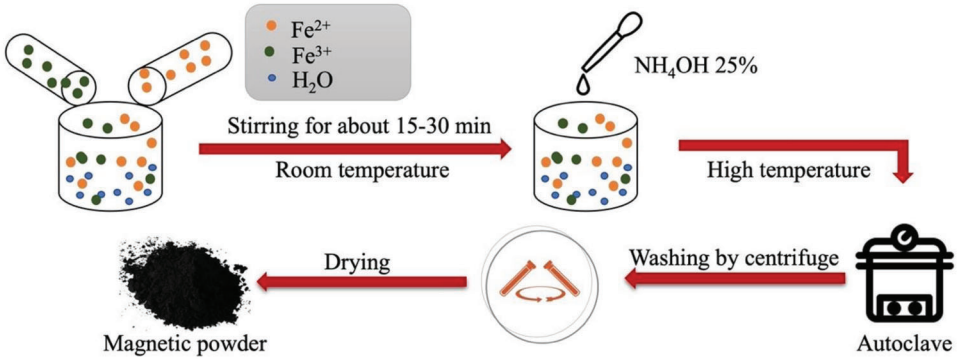

Figure 6. Schematic view of the hydrothermal method.

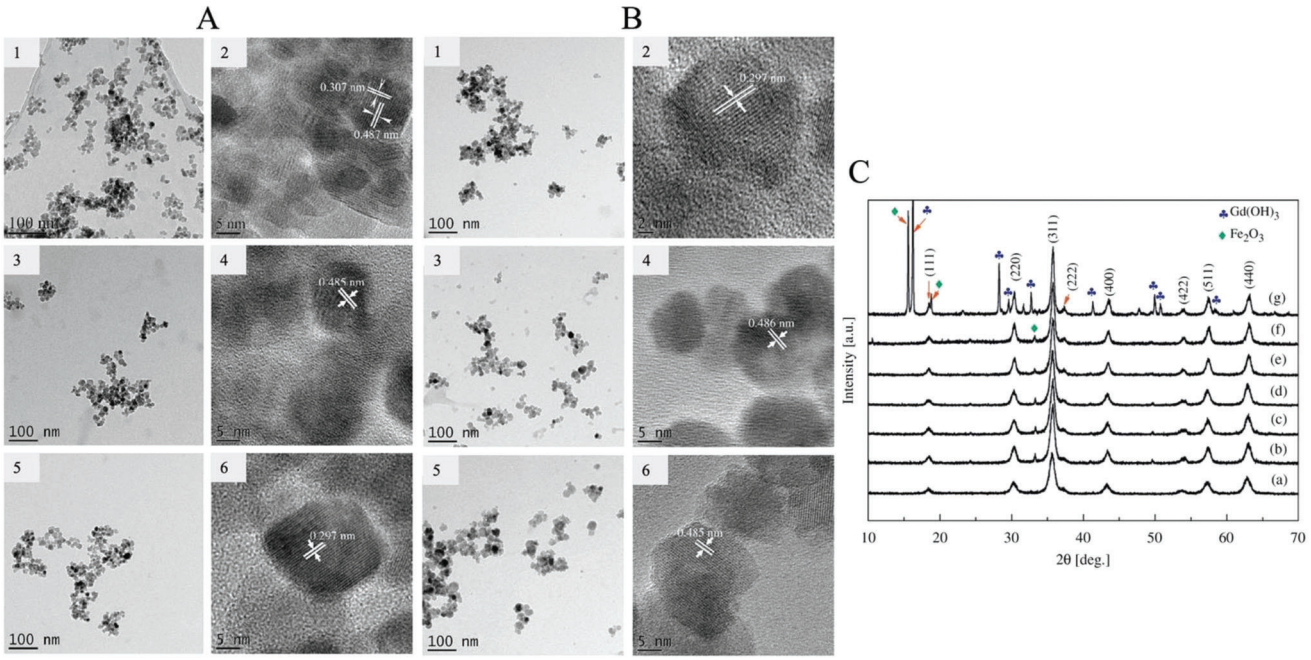

Figure 7. A) TEM and B) HRTEM images of $CoFe_{2-x}Gd_xO_4$ powders: $x = 0$ (1, 2), $x = 0.05$ (3, 4), and $x = 0.10$ (5,6). C) XRD patterns of $CoFe_{2-x}Gd_xO_4$ powders: $x = 0$ (a), $x = 0.05$ (b), $x = 0.10$ (c), $x = 0.15$ (d), $x = 0.20$ (e), $x = 0.25$ (f), and $x = 0.30$ (g). Reproduced with permission.[97] Copyright 2010, Elsevier B.V.

hydrolysis, and condensation reactions during the sol–gel process, including the solvent, temperature, concentration and nature of the salt precursors, pH, and agitation. Although an acid or base can hydrolyze the precursors, water is often the preferred solvent. These reactions take place at room temperature, but additional heating processes are necessary to attain the final crystalline state, and ultimately, the structure and properties of the gel.[96] The sol–gel process is considered one of the most efficient modern technologies for producing a significant quantity of nanoparticles of uniform size.[96,99] In addition, the sol–gel process offers several advantages over other methods, including excellent uniformity, low cost, and high purity in the synthesized MNPs. The process is straightforward, allowing for the precise control of the material structure, and the resulting materials exhibit high chemical reactivity.[99,100] While highly crystalline and uniformly sized magnetite nanoparticles can be produced using

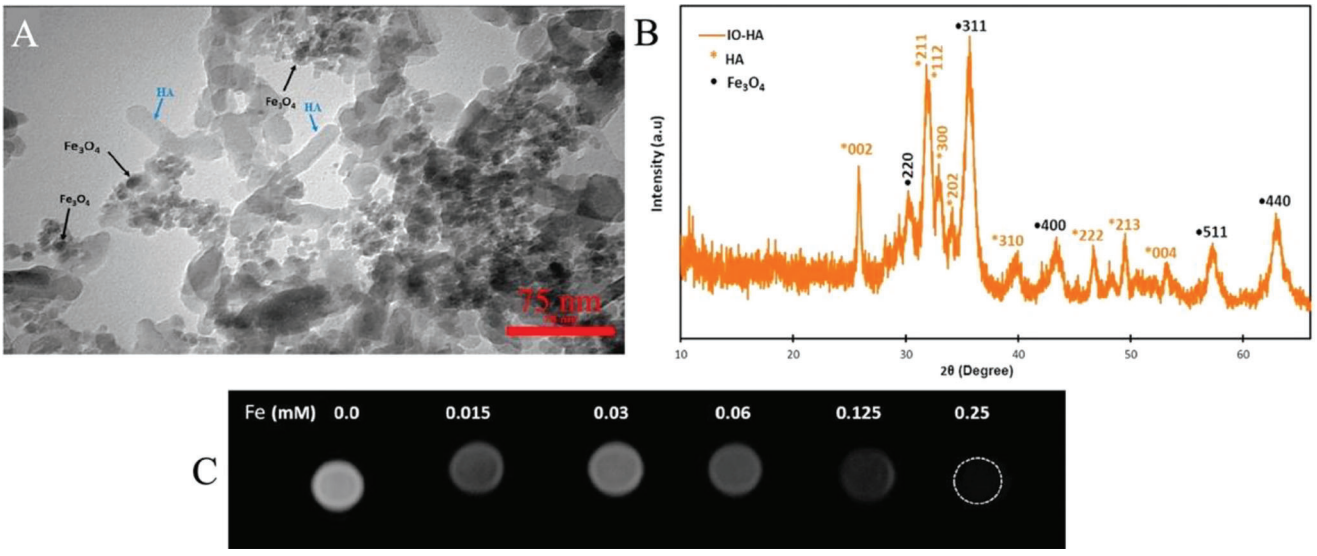

Figure 8. A) TEM image, B) XRD pattern, and C) T2-weighted MRI phantom images of the IO-HA nanocomposite. Reproduced with permission.[98] Copyright 2020, Cell Press.

the sol–gel method, these synthetic approaches are not suitable for large-scale, cost-effective manufacturing due to their reliance on expensive and often hazardous reagents, as well as the complex synthetic stages involved.[100]

Several groups have taken advantage of the benefits of this process for producing various magnetic nanomaterials. For example, Sanpo et al. examined how varying copper concentrations affect the microstructure, crystal structure, and antibacterial activity of copper-substituted cobalt ferrite nanoparticles against *Escherichia coli* and *Staphylococcus aureus*.[101] In their work, citric acid served as the chelating agent in the development of a sol–gel process for synthesizing copper-substituted cobalt ferrite nanoparticles. The resulting nanoparticles had a cubic spinel structure and exhibited a range of morphologies, with crystallite sizes between 35 and 45 nm. Interestingly, increasing the copper concentration resulted in a decrease in both the average particle size and the distribution of particle diameter (refer to Figure 1 of their work). (Authors' note, the MNPs synthesized in their work show irregular cubic shapes and a high degree of agglomeration.) The investigation of the biocidal property of the synthesized ferrite nanoparticles was undertaken utilizing a modified Kirby–Bauer technique. Filter papers, both with and without ferrite nanoparticles, were partially covered and subsequently placed upon a lawn of *E. coli* in an agar plate. The assessment of the contact antibacterial property was performed through the measurement of the clear zone of inhibition surrounding the filter papers following a 24 h incubation period. The antibacterial efficacy of the copper-substituted cobalt ferrite nanoparticles against *E. coli* and *S. aureus* is presented. The introduction of copper into the cobalt ferrite nanoparticles resulted in a slight improvement of the antibacterial activity against *E. coli* but a significant enhancement of the antibacterial activity against *S. aureus*. Furthermore, the incorporation of copper into the cobalt ferrite structure significantly enhanced the nanoparticles' antibacterial properties, potentially enabling it to replace several antibiotics used to treat gastrointestinal problems in animals.

3.4. Thermal Decomposition

Thermal decomposition is considered one of the most important methods for synthesizing MNPs, as the process can be precisely controlled and is already well studied.[102] Studies have demonstrated that alternative methods can be employed for the thermal decomposition of MNPs using inorganic iron precursors such as iron(III) acetylacetonate and iron (0) pentacarbonyl in the presence of hot organic surfactants like oleic acid or oleylamine at high temperatures (≥200 °C).[103] It is found to be highly efficient in producing high-quality IO MNPs with well-controlled sizes. Typically, the MNPs synthesized at higher temperatures have more uniform size distributions. One of the key advantages of this approach compared to coprecipitation is the separation of the nucleation and growth steps, leading to the production of highly crystalline and monodispersed MNPs with a narrow size distribution.[94,104,105] The precise control of the size and morphology distribution of the nanoparticles is dependent on various factors, including the temperature, reaction time, and aging period. The annealing temperatures applied during the synthesis process can enable accurate control over the size and size distribution, as well as the structure and magnetic properties of the resulting nanoparticles.[104]

Numerous studies have reported the synthesis of high-quality MNPs using this method. The work of Patsula et al. focused on the high-temperature thermal decomposition method, specifically the thermolysis of Fe(III) glucuronate under various reaction conditions.[106] The size of the synthesized Fe_3O_4 nanoparticles was confirmed to be 32 nm or smaller, according to the TEM characterization as shown in **Figure 9**A. The Fe_3O_4 spinel phase of the nanoparticles was confirmed by XRD (in Figure 9B), and the saturation magnetization for 11 nm MNPs was determined to be 52.2 $Am^2\ kg^{-1}$. The dispersibility of the Fe_3O_4 MNPs in water is crucial for their use in biomedical applications. To enhance their water dispersibility, a ligand exchange process was employed, which involved binding hydrophilic α-carboxyl-ωbis (ethane-2,1-diyl)phosphonic acid-terminated poly(3-O-methacryloyl-α-D-glucopyranose (PMG-P) to the MNP surface. Under physiological conditions, the PMG-P&Fe_3O_4 aqueous dispersion demonstrated excellent colloidal stability. The physical and chemical properties of PMG-P&Fe_3O_4 nanoparticles make them ideal for in vivo biological and clinical applications, including their potential use as cell labels or MRI contrast agents (Figure 9C).

The same team also synthesized magnetite nanoparticles with a controlled size and a uniform size distribution by a thermal decomposition method.[107] The Fe_3O_4 particles with sizes of 10 (**Figure 10**A:a), 20 (Figure 10A:b), and 31 nm (Figure 10A:c), were synthesized through the process of thermal decomposition of Fe(III) mandelate (3.26 g) in the presence of oleic acid (4.4 g) in octadec-1-ene (40 mL) at a temperature of 320 °C for a duration of 30 min or in icosane (40 mL) at a temperature of 343 °C for a duration of 60 min, respectively. To prevent particle aggregation, the Fe_3O_4 MNP surface was rendered hydrophilic using poly(ethylene glycol) (PEG) with bisphosphonate anchoring groups (PEG-Ner). The hydrodynamic diameters of the Fe_3O_4@PEG-Ner particles with initial 10, 20, and 31 nm sizes were found to be 34, 39, and 62 nm in PBS solution (pH 7.4), respectively, which makes them suitable for most biological applications. In a mouse tumor model, after intravenous administration, most of the 20 nm Fe_3O_4@PEG-Ner nanoparticles were taken up by the liver (Figure 10B). No significant retention of the MNPs in the tumor was observed, even after multiple administrations.

3.5. Microemulsion

Microemulsion refers to a mixture of two immiscible liquids, commonly oil and water, which are stabilized by a third component that acts as a surfactant or a cosurfactant. Surfactants typically consist of organic molecules with a polar head and a hydrophobic tail. These properties enable surfactants to form monolayers at the interfaces between oil and water, with the hydrophilic and hydrophobic groups oriented toward the corresponding phases in order to minimize the electrostatic interaction.[104] When the concentration of surfactant molecules in the mixture reaches a critical point, the surfactants form aggregates known as micelles. The micelle is a spherical structure composed of a hydrophobic core that is shielded from the

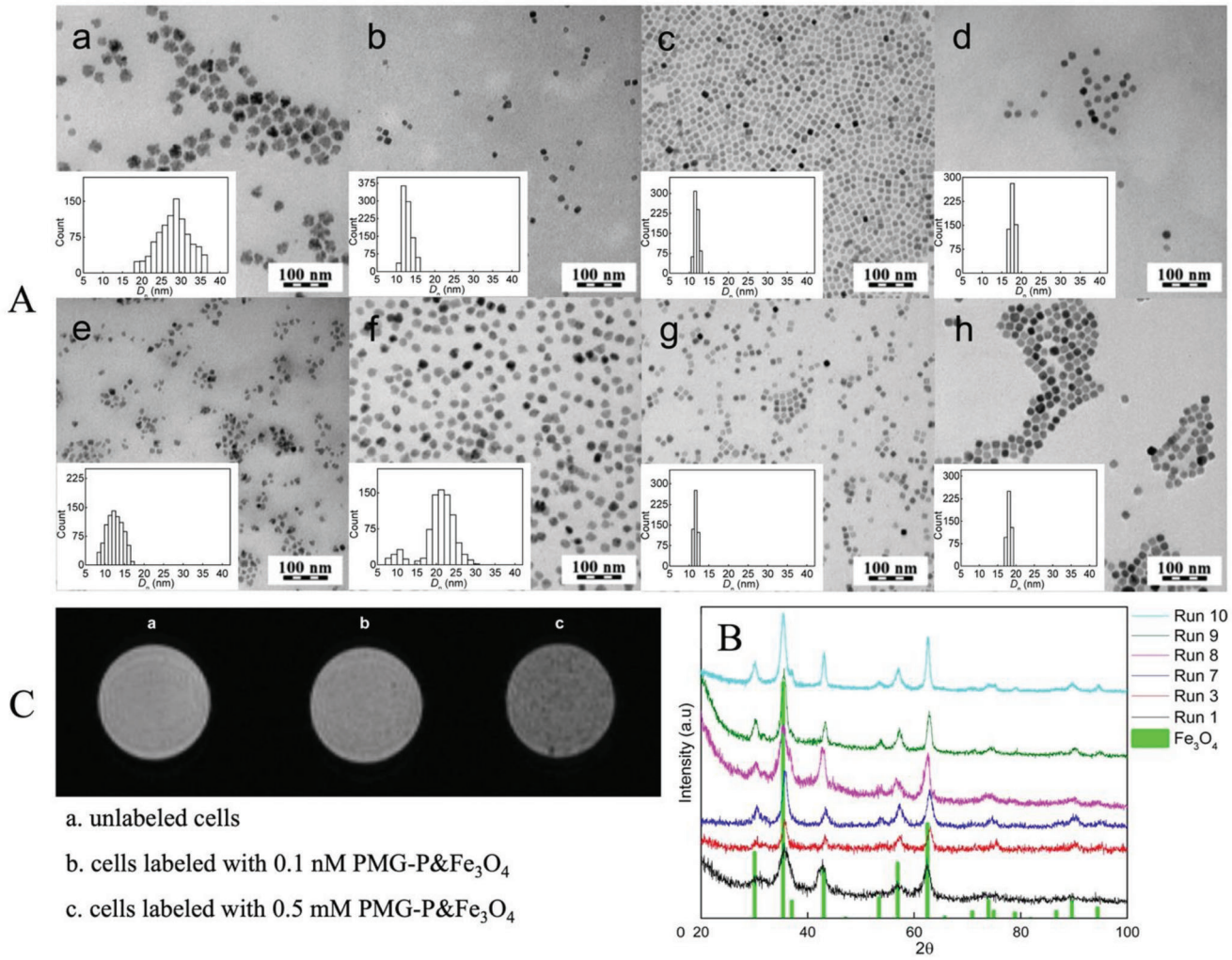

Figure 9. A) TEM images of the Fe_3O_4 MNPs prepared by a high-temperature thermal decomposition method at different conditions: (a,f) in squalene 98% (285 °C), (b) ctadic-1-ene 99% (300 °C), (c,g) ctadic-1-ene 99% (320 °C), (d,h) icosane 99% (343 °C), and (e) monomethyl poly(ethylene glycol) (320 °C). The concentration of oleic acid (OA) was (a–e) 0.15 and (g,h) 0.3 mmol mL^{-1}. B) XRD of the synthesized MNPs. C) MRI cross-sectional T2-weighted images of PMG-P&Fe_3O_4 MNP labeled and unlabeled cells. Reproduced with permission.[106] Copyright 2016, American Chemical Society.

surrounding medium by a hydrophilic shell of surfactant molecules. The hydrophobic tails of the surfactant molecules are directed toward the center of the micelle, while the hydrophilic heads are oriented outward, in contact with the surrounding solvent. This process is spontaneous and thermodynamically favorable, as it reduces the free energy of the system by minimizing the exposure of the hydrophobic tails to the aqueous environment. In a microemulsion, the droplets of one liquid (usually oil) are uniformly dispersed in the other liquid (usually water), forming a clear, transparent solution. This is because the surfactants and cosurfactants present in the system help to stabilize the interface between the two immiscible liquids, allowing for the formation of small, uniform droplets that remain suspended in the continuous phase.[108] The microemulsion method has gained popularity for the synthesis of nanocrystals and nanoparticles because it enables a high degree of control over the reaction. This method allows for precise manipulation of the size, shape, and composition of the nanoparticles by adjusting the parameters of the microemulsion system, such as the concentration of surfactant, the ratio of oil to water, pH, and temperature.[109]

The microemulsion method for synthesizing MNPs offers significant advantages, including precise control over the particle size and shape due to the micelle's stability. The uniform droplet size in the microemulsion system results in the production of nanoparticles with a narrow size distribution, which is highly desirable for many applications.[110] Indeed, the microemulsion method provides several benefits, including high purity and good crystallinity of the nanoparticles, in addition to a narrow size distribution and good control of the particle shape. Additionally, the versatility of this method allows for the synthesis of various types of MNPs, such as CeO_2, Fe_2O_3, Fe_3O_4, ZrO_2, $SrZrO_3$, $LaMnO_3$, among others. This makes it a popular and efficient approach for producing MNPs for a variety of applications. Lastly, the microemulsion method can be performed under mild reaction conditions, usually at room temperature, and requires low energy consumption. This makes the method more environmen-

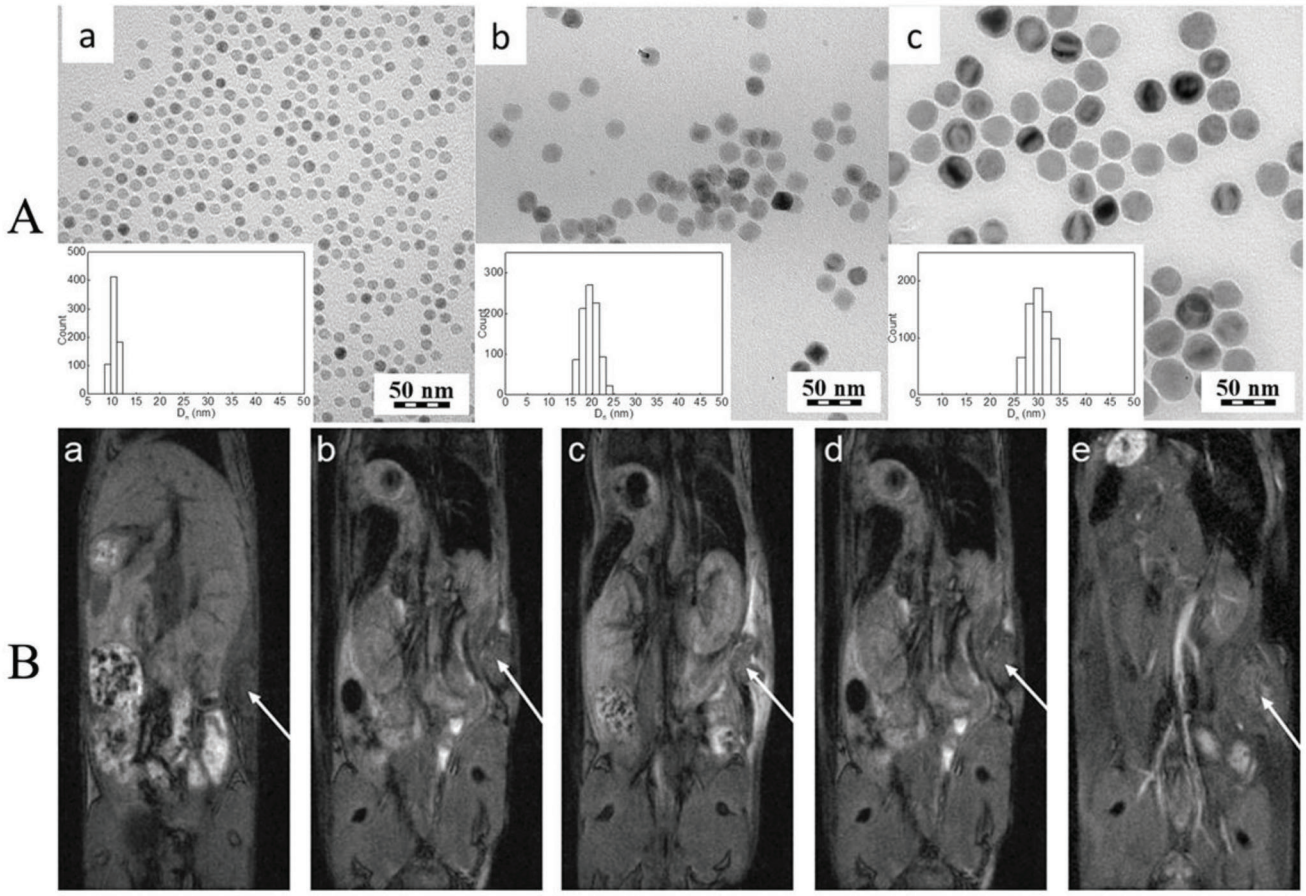

Figure 10. A) TEM images of Fe_3O_4 MNPs: (a) 10, (b) 20, (c) 31 nm Fe_3O_4 particles prepared in (a,b) octadec-1-ene (320 °C) and (c) icosane (343 °C). B) MRI of a mouse with EL-4 tumor (EL-4 (ATCC TIB-39) mouse lymphoma cells) (arrow shows its location): (a) MRI at time 0 (before intravenous administration of Fe_3O_4@PEG-Ner-20 MNPs), (b) at 4 h (4 h after the first dose of 50 µL of Fe_3O_4@PEG-Ner-20 MNPs), (c) at 28 h (4 h after the second dose), (d) at 52 h (4 h after the third dose), and (e) at 120 h (72 h after the third dose). Reproduced under the terms of CC BY 4.0 license.[107] Copyright 2019, Nature Research.

tally friendly and economically feasible compared to other methods that require high temperatures or harsh chemicals.

However, on the downside, the microemulsion method can be time-consuming and requires specialized equipment such as a high-speed homogenizer or an ultrasonic processor. The use of organic solvents in some microemulsion systems may also pose a risk to the environment and human health.[109] Additionally, the separation and purification of the synthesized nanoparticles from the microemulsion can also be challenging, which can lead to contamination and affect the quality of the final product. The stability of the microemulsion system can also be affected by external factors such as changes in the pH or the presence of impurities, leading to inconsistent synthesis results. Finally, the microemulsion method may not be suitable for all types of materials, and alternative methods may need to be employed depending on the specific properties and applications of the desired MNPs.[104]

Nevertheless, this method has rendered good results in the synthesis of several nanomaterials for certain bioapplications. In the study reported by Al-kinani et al., core/shell Fe@Au MNPs were synthesized by the microemulsion method.[111] Au-coated Fe core–shell nanoparticles are a noteworthy variety of nanoparticles that feature a magnetic Fe core enveloped by a fine layer of Au. These nanoparticles exhibited a uniform size of ≈63.65 nm and a spherical form. The dark Fe core and the lighter Au shell could be easily observed in a TEM image, confirming the core–shell structure of the Fe@Au MNPs. This core–shell structure can also provide advantages in drug delivery applications, as it allows for the incorporation of both magnetic and gold properties into a single nanoparticle system, which can enhance drug loading and delivery efficiency.

3.6. Microwave-Assisted Synthesis

Microwave technology has been utilized for the synthesis of MNPs due to its ability to provide quick and uniform heating of precursor ingredients. The penetrating property of microwave irradiation allows for uniform heating of the reaction solution, resulting in uniform crystallization and rapid development of crystallites with a narrow size distribution. The electric and magnetic components of microwaves produce combined

Table 1. Overview of different MNP chemical synthesis methods.

Method	Advantage	Disadvantage
Coprecipitation	– Rapid reaction – Mild reaction conditions – Can be produced in large batches – Low cost – Facile and efficient	– Poor size distribution – Low reproducibility – Surface oxidation – Lack of precise stoichiometric phase control
Hydrothermal	– Superior control in size, shape, dispersion – Does not need calcination step – Magnetic controllability – Excellent crystallinity – Ecofriendly – Low cost	– High temperature and pressure – Longer synthesis time – Pressure–temperature sensitive – Adsorption of capping agents
Sol–gel	– Low cost – Homogeneity – High phase purity	– Formation of secondary phase – Hard to remove the residual organics from porous gel – Post-treatment required
Thermal decomposition	– High yield – Superior size distribution – High reproducibility – Monodispersity	– Safety issues for high temperature and pressure – Solubility in organic solvents – Toxic solvent – Post-treatment required
Microemulsion	– Controllable particle growth, nucleation, and agglomeration – High magnetization values – Simple equipment	– Residual surfactants – Difficult to scale up
Microwave-assisted	– Fast, low-cost, low energy consumption – Uniform shape and size distribution – Especially useful for biomedical imaging	– Slow reaction kinetics – Complicated setup (microwave reactor) required

forces that lead to molecular collisions and friction, which results in a faster reaction time than conventional methods. Therefore, microwave-assisted synthesis can produce uniformly shaped and sized MNPs suitable for biomedical applications, particularly for medical imaging.[112,113]

According to the work of Brollo et al., microwave-assisted synthesis plays a critical role in preparing outstanding magnetic IO nanoparticles.[114] The experimental parameters, such as the solvent, precursor, and surfactant, significantly influence the nucleation and growth processes, and thus, ultimately determine the particle size and uniformity. Unlike conventional heating methods, microwave heating provides effective internal heating, promoting nucleation throughout the reaction solution and limiting the potential development of multiple nuclei. Research has shown that magnetic IO nanoparticles with diameters ranging from 8 to 15 nm can be achieved with this method, and particles exhibit superparamagnetic behavior when synthesized through microwave and thermal decomposition in organic environments, making them suitable candidates for MRI negative contrast agents.[114] The small hydrodynamic sizes of these nanoparticles, combined with their Ms, appear to be the primary factors dictating their effectiveness as MRI contrast agents.

3.7. Overview of MNP Chemical Synthesis Methods

In **Table 1**, we have compared the advantages and disadvantages of various MNP synthesis methods reviewed in this section.

4. Surface Functionalization of MNPs

MNPs require a biocompatible surface coating that enhances their ability to adsorb, covalently attach, and bind to target molecules for biomedical applications. Surface functionalization serves to preserve the original structure of the MNPs and prevent agglomeration due to interparticle attraction, as well as to prevent further biodegradation. In this section, we will review several inorganic and organic coating strategies that are frequently used on MNPs.

4.1. Inorganic Coating

Surface functionalization of MNPs can be achieved by coating them with various inorganic substances such as gold and silica, which not only provides enhanced stability to the MNPs in solution but also plays a crucial role in enabling the attachment of biological entities to the MNP surface.[115]

4.1.1. Silica Coating

Encapsulating MNPs in a silica shell is a commonly used and promising method for creating stable and biocompatible nanostructures for biomedical applications.[115,116] In general, silica is known for being optically transparent, chemically inert, thermally stable,[117] with a well-established surface chemistry, high processability, and controlled porosity.[118] These properties make it an ideal material for biomedical applications, as it can prevent toxicity, improve chemical stability and biocompatibility,[117] and inhibit particle aggregation.[116]

The formation of core/shell silica-coated MNPs always results in water-soluble, colloidally stable, and photostable particles.[119] The excellent colloidal stability can be attributed to two main factors. First, cations and positively charged molecules can strongly

interact with the unique silicate layer at silica–water interfaces, especially under basic conditions. Second, compared to other nanoparticles, the van der Waals interactions are relatively weak due to their lower Hamaker constant.[118] The stability of the MNPs can be enhanced by utilizing the silica shell as a buffer against magnetic dipole interactions (which is especially useful in high MNP density scenarios) or by boosting the columbic repulsions of the MNPs which helps to prevent agglomeration.[115] In addition, the surface of silica-coated MNPs provides silanol groups that can readily react with alcohols and silane coupling agents to form dispersions that are stable not only in nonaqueous solvents but also serve as an excellent anchor for covalent attachment of specific ligands. The strong binding affinity of these ligands to the silanol groups makes it difficult to desorb them.[120] Functionalizing silica-coated MNPs with carboxyl, thiol, and amine groups can make them suitable for various biomedical applications. These functional groups can be further modified with drugs and enzymes for specific biomedical applications. Thus, MNPs coated with silica can also be used for bioseparation, enzyme immobilization, and diagnostic testing.[121]

4.1.2. Gold Coating

The surface of MNPs can be modified with biocompatible gold to stabilize the nanoparticles in water, prevent particle aggregation, and allow for the attachment of various ligands.[122] MNPs have a high surface-to-volume ratio and possess magnetic properties that make them highly attractive for a range of applications. However, one of the challenges associated with the use of MNPs is their tendency to aggregate, leading to opsonization and reduced stability. When MNPs aggregate, they become less stable and can clump together, limiting their effectiveness in various applications. This issue is particularly problematic in biological systems, where MNPs may be used for drug delivery or imaging purposes.[123] One solution to these challenges is to coat the MNPs with gold. This coating not only shields the magnetic core but also improves conductivity, optical properties, biocompatibility, bioaffinity, and chemical stability. The resulting Au@MNP hybrids are highly adaptable, with their properties easily adjustable by altering the size, thickness of the gold shell, shape, charge, and surface modification of the particles. These improvements have broadened the potential applications of Au@MNPs to various biomedical fields. Indeed, the excellent biocompatibility of Au@MNPs makes them suitable for drug delivery, imaging, and biosensing. On the other hand, the gold layer enhances the light absorption capabilities of the MNPs, making them ideal for applications in which strong light absorption is required.[124] The surface plasmon resonance phenomenon on the gold coating surface enables MNPs to exhibit strong absorption and scattering of near-infrared (NIR) wavelengths, resulting in enhanced Raman scattering (i.e., surface enhanced Raman scattering or SERS), which allows light to penetrate human tissue more deeply.[122,125] Overall, the gold coating of MNPs has proven to be an effective way of overcoming the limitations of bare MNPs and has expanded the range of applications in which these materials can be used.[126]

In recent years, the use of gold-coated MNPs (Au@MNPs) has gained recognition in the field of analytical chemistry. One area where Au@MNPs have shown promise is in bioseparation, where their unique properties make them ideal for separating and purifying biological molecules. In addition, Au@MNPs have been used in the development of electrochemical and optical sensors for the detection of a wide range of analytes. The excellent biocompatibility of Au@MNPs also makes them well-suited for targeted drug delivery. Moreover, the magnetic properties of Au@MNPs make them suitable as contrast agents for MRI. The development of new and innovative uses for these materials is an active area of research, and ongoing efforts are aimed at improving their performance and expanding their range of applications.[126]

Another promising application of Au@MNPs is in photothermal tumor therapy. Superparamagnetic iron oxide nanoparticles (SPIONs) with gold-modified surfaces have been identified as potential candidates for this type of therapy due to their strong absorption in the NIR electromagnetic band. When irradiated with NIR light, these particles generate heat that can be used to destroy cancerous cells. Furthermore, studies have shown that MNPs with a gold surface exhibit reduced cytotoxicity against healthy cells, making them a safer option for cancer therapy. These properties make Au@MNPs attractive for this application and have prompted ongoing research aimed at optimizing their performance in this field. Overall, the combination of magnetic and gold properties in Au@MNPs has opened up new possibilities for the development of novel cancer treatments that offer improved efficacy and safety.[123]

4.2. Organic Coating

4.2.1. PEG Coating

PEG is a synthetic linear polymer that exhibits both hydrophilic and hydrophobic properties and can be synthesized with a variety of terminal functional groups. These functional groups can be modified to enable PEG to bind to different surfaces. PEG has been widely employed as a coating material in a variety of biotechnological applications due to its distinctive properties, which include water solubility, biocompatibility, flexibility, nontoxicity, and nonantigenic behavior. These features make PEG a versatile and valuable material in a wide range of biomedical applications, including drug delivery, tissue engineering, and bioconjugation. Additionally, PEG is well-known for its ability to reduce protein adsorption and minimize the immune system recognition.[127] PEG has also been extensively studied as a surface coating material for MNPs. One of the key advantages of using PEG as a coating material for MNPs is its ability to prevent opsonization in the blood (opsonization occurs when proteins in the blood bind to the surface of MNPs, leading to their recognition and removal by the immune system), which can significantly prolong the particles' circulation time in the bloodstream. PEG coating of MNPs has been shown to reduce protein adsorption, decrease the binding of antibodies, and minimize the risk of immune recognition, thereby improving the material's biocompatibility and circulation time in vivo and enhancing the targeting of specific tissues or cells.[122,128]

The extended circulation time of PEG-coated MNPs in living systems, coupled with their ability to be readily eliminated through the kidneys, has further increased their theragnostic potential. PEG-coated MNPs have been shown to have high specificity and sensitivity for detecting and treating diseases, such as cancer, cardiovascular disease, and neurological disorders. The ability of PEG-coated MNPs to evade the immune system and remain in circulation for longer periods of time can improve their efficacy as diagnostic and therapeutic agents. Additionally, their easy renal clearance minimizes the potential for accumulation and toxicity in the body, which is a crucial factor for the safety of any therapeutic agent. In conclusion, PEG-coated MNPs hold great potential as theragnostic agents, and their properties make them an attractive option for a range of biomedical applications.[128]

4.2.2. Dextran Coating

Dextran is also a commonly applied coating layer to functionalize MNPs due to its nontoxic, biocompatible, water-soluble, and degradable properties. Coating MNPs with dextran has been shown to improve their colloidal stability and ability to deliver drugs.[127,129] Moreover, dextran-coated MNPs are widely used in critical applications such as MRI and hyperthermia,[130] cellular targeting probes,[130] cancer imaging, and therapies. Dextran-coated SPIONs have been approved for clinical use in MRI of the liver because they effectively prevent nanoparticle aggregation.[124]

Experiments conducted to determine the biocompatibility of dextran-coated MNPs have shown that the surface-immobilized dextran remains stable in most tissue environments, as it is resistant to enzymatic degradation.[122] Human cell lines are unable to synthesize dextranase, which is the enzyme responsible for degrading dextran. This is why dextran-coated MNPs are considered stable in most tissue environments.[124] Dextran is a hydrophilic polymer composed of multiple glucose monomers linked together by α-1,6-glycosidic bonds. When exposed to alkaline solutions, dextran can physically adsorb onto MNPs through noncovalent bonding. Using carboxymethyl dextran (CMD), a derivative of dextran, to create MNPs provides functional groups with both hydroxyl and carboxyl groups, which makes chemical modification easier. CMD possesses excellent biocompatibility, biodegradability, and high water solubility.[127] However, one of the key drawbacks of dextran coating is the weak binding between dextran and the surface of MNPs. This could have a significant impact on the effectiveness of dextran-coated MNPs in various applications.[124]

4.2.3. Chitosan Coating

Chitosan is a cationic polysaccharide with a structure like that of cellulose, consisting of glycosidic linkages and 2-amino-2-deoxy-h-d-glucan. Its primary amine groups have made it a popular choice for pharmaceutical applications. Additionally, chitosan's positive charge and mucoadhesive properties make it well-suited for drug delivery applications. However, chitosan is not soluble in water at basic or neutral pH levels.[124] It is worth noting that at acidic pH levels, the amino groups in chitosan become protonated, which makes chitosan water soluble.[131] Chitosan is not only water-soluble at acidic pH levels, but it is also biodegradable, with the degradation products being nontoxic amino sugars. This polymer is affordable and has been shown to have no immunogenic or allergic effects on the body.[122] Furthermore, chitosan can adsorb harmful substances and possesses antibacterial qualities, in addition to its adhesion and immunostimulatory properties. These characteristics make it well-suited for magnetic bioseparation and affinity protein purification applications.[132] These unique characteristics of chitosan have made chitosan-coated MNPs an attractive option for a variety of tissue engineering applications.[124]

As a summary, **Figure 11** shows TEM images of MNPs that are coated with different organic and inorganic layers.

5. Biomedical Applications of MNPs

5.1. MNPs for MRI

MRI is an incredibly effective bioimaging technology that produces high-quality images of the internal organs of the human body. It has a vast range of applications in treating patients with various conditions such as organ inflammation or infection, degenerative illnesses, strokes, musculoskeletal problems, tumors, and other anomalies in body tissue or organs.[136] Compared to computerized tomography (CT) scan, MRI is a noninvasive method for obtaining images of an object in the body. It relies on the relaxation process of proton nuclei in water and lipids to show high-resolution images with exceptional soft tissue contrast between different tissues. With extreme imaging flexibility, nonionizing radiation, patient harmlessness, and high patient acceptance, this technique offers numerous advantages. Additionally, it provides physiological parameters and specific clinical information for better diagnosis and treatment.[137,138] Although it can detect and identify tumors more clearly and quickly, the inherent low sensitivity of this test makes it challenging for clinicians to differentiate normal and abnormal tissues.[139] MRI is a versatile imaging technique that allows for both diagnostic radiology and therapeutic medicine. It uses multiple relaxation processes, including longitudinal (T1) and transverse (T2) relaxation, to create images of the body. However, the images obtained by MRI alone may not be sufficient for certain applications, such as tumor detection and tracking. Contrast agents, such as MNPs, can be used to enhance the accuracy and clarity of images, enabling physicians to better detect abnormal tissues or organs.

T1, which is also referred to as spin-lattice relaxation time, refers to the rate at which the net magnetization vector (NMV) returns to its original state aligned with the direction of the main magnetic field (B_0). In the case of tissue, the typical value for T1 is $\approx$1 s.[137] T2 relaxation, also known as spin–spin or transverse relaxation, refers to the attenuation of a signal with time. During T2 relaxation, high- and low-energy spin states exchange energy without releasing energy to the surrounding lattice. Once the nuclei release their excess energy, the magnetic moments interact with one another, leading to a decrease in transverse magnetization, namely, signal attenuation. For most tissues, T2 typically has a value below 100 ms. MRI image contrast is commonly

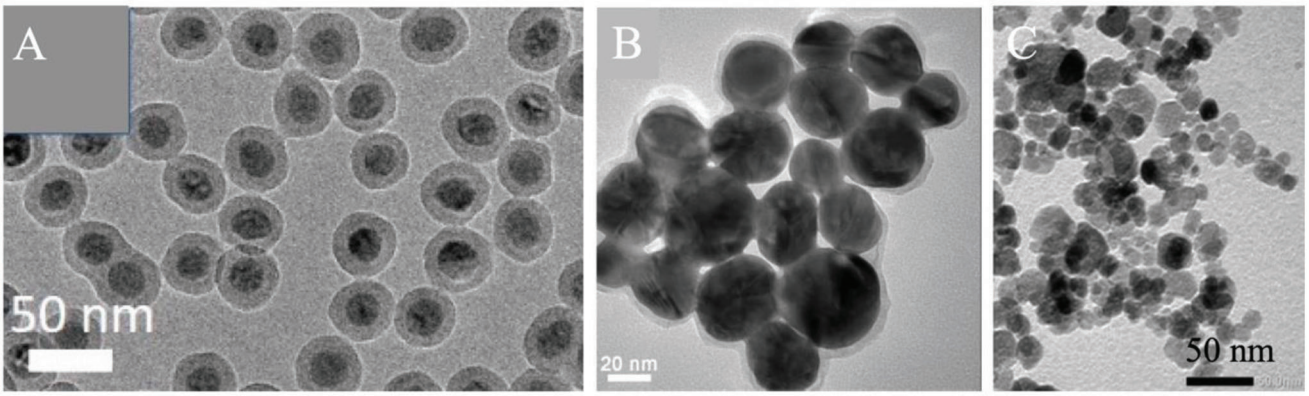

Figure 11. TEM images of MNPs with inorganic and organic coatings. A) Silica coating. B) Gold coating. C) PEG coating. (A) Reproduced under the terms of the CC BY 4.0 license.[133] Copyright 2020, MDPI. B) Reproduced with permission.[134] Copyright 2007, Wiley-VCH GmbH & Co. KGaA, Weinheim. C) Reproduced under the terms of the CC BY 4.0 license.[135] Copyright 2020, IOP Science.

categorized based on the sensitivity of the three tissue factors: proton density (ρ), longitudinal (or spin–lattice) relaxation time T1, and transverse (or spin–spin) relaxation time T2. A proton-density-weighted image is a sequence that is mainly sensitive to the ρ parameter. T1- or T2-weighted images, respectively, are image sequences that are predominantly sensitive to T1 or T2 relaxation times. Contrast agents play a crucial role in enhancing MRI contrast. These are a special class of drugs that improve the contrast between healthy and diseased tissue on an image and reveal the condition of organ function or blood flow after treatment by increasing the rates at which water protons relax in tissue where the agent accumulates. Paramagnetic substances, which have a net positive magnetic susceptibility, and superparamagnetic and ferromagnetic materials, which become magnetized in the presence of an external magnetic field, have very large net positive magnetic susceptibilities and are used as MRI contrast agents.[140]

5.1.1. T1-Contrast Agents for MRI

Positive contrast agents, known as T1 agents, typically increase longitudinal (or spin–lattice) relaxation rates of water protons in tissue to a greater extent than transverse (or spin–spin) relaxation rates (1/T1), on a percentage basis. These agents cause an increase in signal intensity that is predominantly observed on T1-weighted images, using the majority of typical pulse sequences.[140] The T1 relaxation time is not constant and varies depending on the biological system. Positive imaging can be achieved using T1 contrast agents, which can discriminate between fat and water, with fat showing a brighter contrast and water exhibiting a darker contrast. In the presence of paramagnetic materials, the T1 relaxation time is shortened.[136]

Paramagnetic contrast agents are typically composed of the lanthanide metal gadolinium (Gd^{3+}) or the transition metal manganese (Mn^{2+}), which is capable of dispersing in water. Among these, Gd^{3+}, with the most stable configuration of unpaired electrons and a strong magnetic moment, is the metal atom most commonly used as an MRI contrast agent.[141] Paramagnetic contrast agents exhibit their contrast-enhancing properties due to the presence of unpaired electrons. Gadolinium, for instance, has seven unpaired electrons while manganese has five. Contrast agents containing gadolinium are known to reduce the T1 (longitudinal relaxation) and T2 (transverse relaxation) times of nearby water protons. These effects lead to an increase in the signal intensity of T1-weighted images and a decrease in the signal intensity of T2-weighted images.[137,141] While Gd^{3+} cations have a shorter circulation time as a T1-weighted MRI contrast agent, this limits their utility for high-resolution and/or targeted MRI applications.[142] Additionally, there are concerns regarding the potential gadolinium ion deposition in the body, which can lead to a condition called nephrogenic systemic fibrosis (NSF).[143] NSF is a rare disease that often occurs in patients with severe renal failure or after liver transplantation with or without dialysis. Despite this risk, Gd-based contrast agents remain effective at shortening the relaxation time and providing brighter images in regions of interest.[144] Due to the increasing awareness of the negative side effects associated with gadolinium-based contrast agents, researchers are placing greater emphasis on alternative techniques based on Mn-based complexes. While studies have shown that there is no scientific link between NSF and Mn, the metal is still considered to be toxic when inhaled. Although small amounts are necessary for human health, excessive exposure to free Mn^{2+} can cause "manganism", a neurodegenerative disease with symptoms similar to Parkinson's disease.[145]

Gd-based MNPs have been successfully employed as novel contrast agents for several applications. Lim et al. conducted a study on pyrene-Gd (Py-Gd) MNPs as a novel T1 MRI contrast agent that has the potential to produce highly sensitive images in a cancerous environment (see **Figure 12**A).[146] The size of the samples observed from TEM images was ≈216.78 ± 4.9 nm (Figure 12B). Py-Gd MNPs showed significant MRI signals when Gd ions were exposed to acidic conditions (pH 5.5) compared to neutral conditions (pH 7.4) after incorporating pyrenyl PEG into the material as more interactions occurred between the Py-Gd and the pyrenyl PEG pyrene groups at lower pH values. The Py-Gd MNPs demonstrated their potential as MRI agents for cancer diagnosis via the enhanced permeability and retention effect in both in vitro and in vivo scenarios, as they

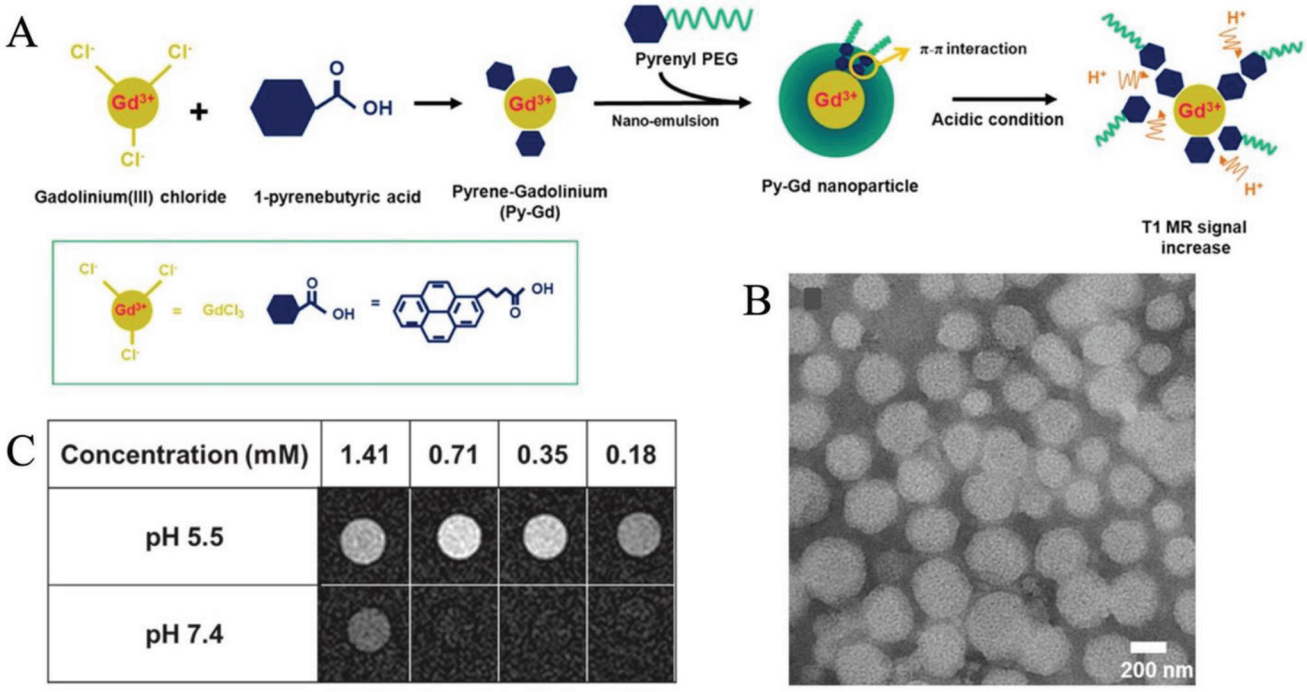

Figure 12. A) Schematic illustration of the preparation of Py–Gd nanoparticles as pH-sensitive T1 MRI contrast agents. B) TEM image. C) T1-weighted images. Reproduced with permission.[146] Copyright 2014, IOP Publishing Ltd.

were able to clearly enhance the images with high MRI signals (Figure 12C).

5.1.2. T2-Contrast Agents for MRI

T2-weighted images are sequences in which structures with long T2 relaxation times appear bright, while those with short T2 relaxation times appear dark. T2 agents shorten the T2 relaxation time of nearby water protons, which causes a decrease in signal intensity and a decrease in the brightness of the corresponding tissue on T2-weighted images. Therefore, T2 agents are referred to as negative contrast agents.[140] The presence of contrast agents containing SPIONs significantly affects the T2 relaxation. These contrast agents are considered negative contrast agents because they selectively increase the tissue's 1/T2 while decreasing the signal intensity, which is particularly evident in T2-weighted images.[147] SPIONs reduce the T2 relaxation time of nearby water protons, leading to a decreased signal intensity and darkening of images on T2-weighted images due to their large size and magnetic moment, which cause efficient spin dephasing and transverse relaxation of nearby protons by an outer-sphere mechanism. The protons experience this effect as they diffuse through the microscopic magnetic field gradients around such particles. These agents are commonly used in clinical practice for various imaging applications.[140,148] However, it has also been claimed that a new generation of ultrasmall superparamagnetic iron oxide nanoparticles with diameters less than 10 nm have excellent T1-enhancing characteristics suggesting that this approach could be employed for creating dual/weighted contrast agents.[140,141]

MNPs have been focused on intense research in this field. Mohammadi et al. employed a coprecipitation method to synthesize superparamagnetic $CoFe_2O_4$ nanoparticles.[149] An HRTEM image of the synthesized $CoFe_2O_4$ MNPs showed a nonuniform and heterogeneous morphology of the material with an average size of 10.45 nm (**Figure 13**A). Also, the structural analysis obtained from the XRD pattern indicated that the $CoFe_2O_4$ MNPs had an inverse cubic spinel-type. The T1 and T2 relaxation times of hydrogen protons in solutions of different concentrations of $CoFe_2O_4$ MNPs in water were calculated using traditional MRI. The calculated T1 and T2 relaxation rates (r_1 and r_2) were 1.15 and 58 $mM^{-1}\ s^{-1}$, respectively. These results suggest that the synthesized MNPs could be used as negative contrast agents at low concentrations in a conventional MRI system due to the high r_2/r_1 value (Figure 13B). The $CoFe_2O_4$ MNPs were also found to be a suitable contrast agent for cell labeling, with the best performance observed at a concentration of 0.154 mM, which falls within the nontoxic concentration range. In vitro cell viability tests showed that $CoFe_2O_4$ MNPs did not reduce cellular viability up to a concentration of 0.75 mM (see Figure 13C). Therefore, the authors suggest that $CoFe_2O_4$ MNPs can be considered a theragnostic agent.

5.2. MNPs for MPI

MPI is an imaging technique that employs MNPs as tracers to create precise and highly sensitive tomographic images for a wide range of areas, including neuroimaging, tumor imaging, cardiovascular imaging, and cellular tracking.[150] In 2001, Gleich and Weizenecker first reported the idea of MPI, and it was later

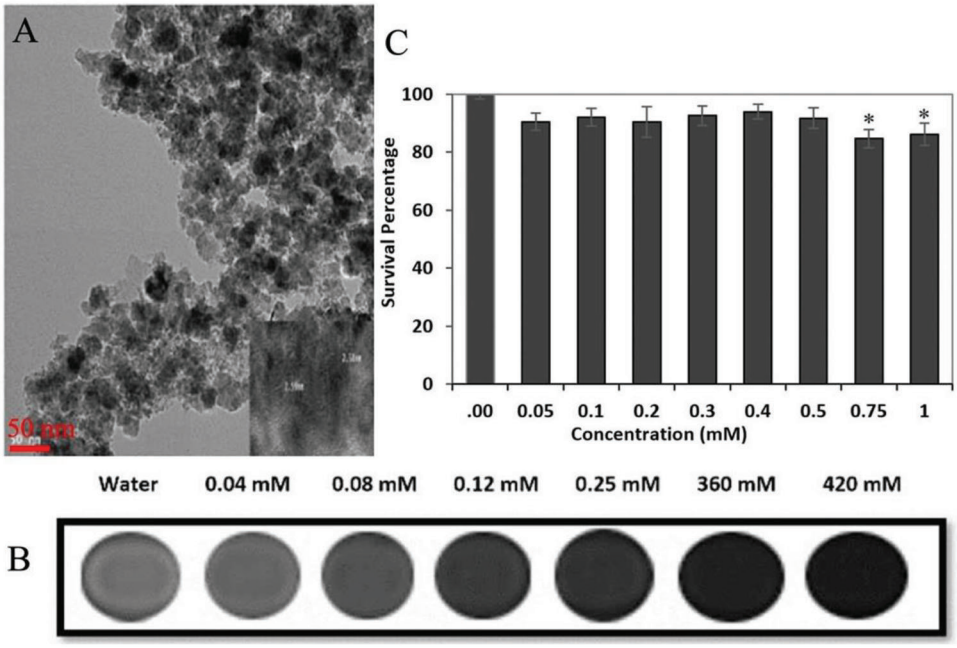

Figure 13. A) HRTEM of $CoFe_2O_4$ MNPs. B) T2-weighted image of $CoFe_2O_4$ MNPs in a water medium obtained by a conventional spin-echo pulse sequence on a 1.5 T MRI system. C) In vitro cytotoxicity of $CoFe_2O_4$ MNPs tested on a KYSE 30 cell line for 24 h by an MTT (3-(4,5-dimethylthiazol-2-yl)-2,5-diphenyltetrazolium bromide) assay. The * sign indicates the significance of the statistical test. Reproduced with permission.[149] Copyright 2020, The Institution of Engineering and Technology.

introduced to the public in 2005 as a possible way to quickly image the small intestine and blood vessels.[151] MPI can be used either together with other imaging methods like MRI or CT or in its own.[152,153]

At the heart of MPI lies the interaction between MNPs and a time-varying magnetic field.[154] The field of view defines the region of interest in the imaging process, while the field-free point (FFP) represents a spatial location where the DC magnetic field is zero. The field-free line (FFL) connects multiple FFPs and serves as the pathway for spatial encoding during imaging. The gradient field is utilized to create the necessary spatial encoding within the FFP/FFL, while the exception field supplements the system by introducing an additional magnetic field to suppress the tracer signals outside the FFP/FFL.[155] The receiver coil captures the induced signals from the excited MNPs, enabling their detection and subsequent imaging. Within the FFP, MNPs are subjected to a unique composite field consisting of a 0 DC field and an excitation field. This field configuration is significant in the context of MPI as it enables the detection and quantification of the MNPs' nonlinear magnetization responses. The presence of the 0 DC field ensures the absence of an external static magnetic field that could influence the MNPs, while the excitation field induces the desired magnetization dynamics on the particles. The resulting nonlinear magnetization responses arising from the interplay between these two fields are recorded as the MPI signal. The MPI signal acquired from MNPs located within the FFP provides valuable insights into their characteristics, including their concentration and spatial distribution within the imaged region. By contrast, MNPs positioned outside the FFP experience a distinct field environment. In this scenario, a DC selection/gradient field is applied alongside an exception. The primary purpose of the selection field is to fully saturate the magnetizations of the MNPs, thereby rendering them immobile and devoid of any dynamic magnetizations. Consequently, when examining the MPI signal, no discernible contributions from MNPs located outside the FFP can be observed or quantified.[156] To summarize, the provided description elucidates the divergent responses exhibited by MNPs within and outside the FFP in the context of MPI. The FFP configuration enables the detection of nonlinear magnetization responses, culminating in the generation of the MPI signal. Conversely, MNPs situated outside the FFP undergo magnetization saturation due to the nonzero selection field, resulting in the absence of dynamic magnetizations and hence their noncontribution to the MPI signal.

Certain antibodies or peptide sequences can be added to the surface of MNPs to enable accurate targeting of cancer cells. Du et al. have utilized tumor targeting agents such as CREKA (Cys–Arg–Glu–Lys–Ala amino acids) to functionalize PEG-coated IO nanoparticles.[157] They introduced CREKA as a pentapeptide that binds to fibrin–fibronectin complexes expressed by cancer cells. By functionalizing MNPs with CREKA, the particles could selectively accumulate within cancer cells after systemic administration, as shown in Figure 15A. In their study, they administered 50 µL of 0.5 mg mL^{-1} 18 nm iron oxide NPs (IOs) or Vivotrax (a SPION tracer) intratumorally, ensuring an equal Fe content. To monitor the changes in the signal over time, they employed MPI and MRI techniques. The results revealed that the synthesized IOs exhibited a significantly higher MPI signal compared to Vivotrax, ranging from 4 h to 14 days postinjection. Notably, they observed that the MPI signal enhancement of the nonfunctionalized IOs was limited to the injection site rather than being uniformly distributed throughout the tumor. **Figure 14**A clearly

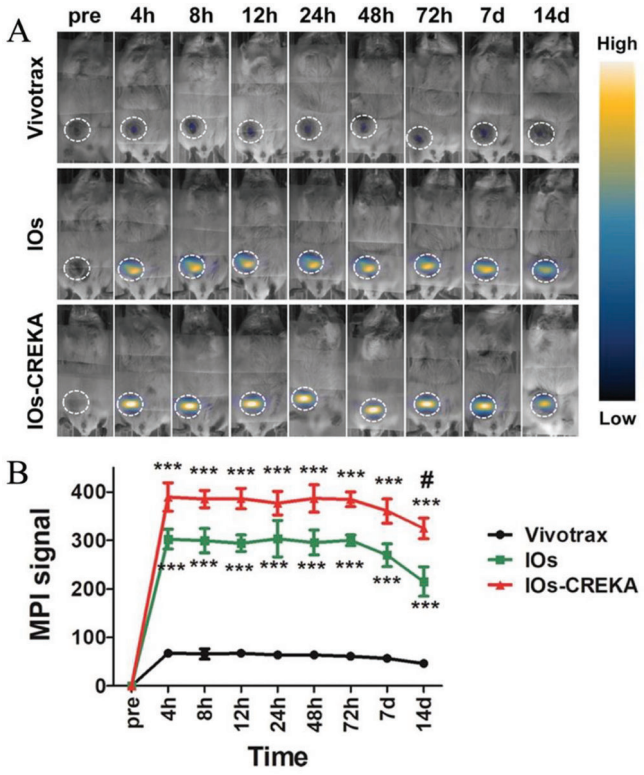

Figure 14. Figure generated by combining MRI and MPI scans, which shows the distribution of nanoparticles within a mouse model. A) Enhancement of the MPI signal intensity utilizing CREKA functionalized IOs nanoparticles. B) Comparison of the MPI signals over time for IOs-CREKA, IOs, and Vivotrax groups. Reproduced with permission.[157] Copyright 2019, American Chemical Society.

demonstrates the MPI image highlighting the injection site with minimal MNP distribution within the tumor. To enhance intratumoral delivery, CREKA-conjugated MNPs were utilized, which specifically target fibronectin—a highly expressed component in the breast tumor microenvironment. Additionally, as presented in Figure 14A, evidence of improved intratumoral distribution was achieved using targeted IOs-CREKA MNPs. From as early as 4 h postinjection, a higher and more uniform MPI signal throughout the entire tumor region was observed, in contrast to the nonconjugated IOs group. For instance, at day 14 postinjection, the MPI signal intensity of the functionalized IOs-CREKA group was 1.526 ± 0.119-fold higher than the nontargeting IOs group, and 5.700 ± 0.581-fold higher compared to the Vivotrax group (Figure 14B).

5.3. MNPs for Hyperthermia Therapy

Less aggressive and more effective cancer treatments are needed because the currently employed methods, such as chemotherapy and radiotherapy, might harm the human body in unintended ways.[158] Among the different types of therapies, in hyperthermia body tissue is exposed to high temperatures[159] in order to harm and kill cancer cells or to make cancer cells more susceptible to the effects of radiation and specific anticancer drugs.[160] Two different heating techniques have been used up to date: 1) hyperthermia at temperatures between 41 and 45 °C, and 2) thermoablation at temperatures higher than 45 °C for the local induction of tissue necrosis.[161] For hyperthermia applications, the heating sources are typically positioned outside the body (e.g., antennas) to locally emit electromagnetic waves into the tumor location (microwaves or radiowaves). These methods need the tumor's location in the relevant organ to be identified beforehand by the appropriate imaging techniques.

Whole-body heating is advised in contrast when carcinomas with distant metastases are present.[162] These techniques have serious limitations when it comes to precisely targeting tumors or localizing heat energy. The entire body is heated over the normal physiological temperature in whole-body hyperthermia, while techniques using the remote delivery of electromagnetic radiation are nonetheless tissue nonspecific. Its wavelength also limits the accuracy, which causes substantial heating of the tissues around the target tumors or insufficient heating.[162] Thus, research has focused on magnetic fluid hyperthermia because by utilizing MNPs, a strong energy focus can be achieved in the tumor location. Utilizing MNPs in an external AC magnetic field offers a promising approach in the treatment of cancer, as it enables targeted delivery of heat exclusively to the cancerous region while avoiding the surrounding healthy tissue.[161] This is achieved through specific magnetization processes that occur when the MNPs are exposed to alternating magnetic fields, resulting in controlled heating. Magnetic hyperthermia, as a result, emerges as a highly favorable technique for cancer treatment.[158]

When MNPs with high Ms are used, heat will be generated to increase the effectiveness of hyperthermia. MNPs can technically be administered locally or through the intravascular region near an external alternating current magnetic field.[163] An essential factor that primarily determines the dosages that must be administered to the tumor location to reliably inactivate target cells is the heating potential of the nanoparticles (i.e., the specific absorption rate, SAR). The heating potential is determined by the amount of heat that results from the exposure of the nanoparticles to an alternating magnetic field per unit of mass and time.[161] In general, one of the three separate mechanisms, hysteresis loss, Brownian relaxation, and Néel relaxation, can result in heating magnetic materials with high-frequency magnetic fields.

The different heating delivery systems depend on the morphological characteristics of the magnetic material (nanoparticle size, shape, and microstructure),[161] the effective anisotropy constant K_{eff}, M_S, as well as the medium viscosity (η).[164] Heating is provided by displacements of the domain wall for multidomain MNPs (with sizes above 40 nm depending on the material).[165] Superparamagnetic nanoparticles, by contrast, are suspensions of nanoparticles with diameters less than ≈40 nm (depending on the material). For these smaller particles, heat is generated as a result of frictional losses when the nanoparticle is able to rotate in the surrounding media (Brownian relaxation) or loss processes during the reorientation of the magnetization (Néel relaxation) in the magnetic field.[159,166] When a material is exposed to an AC magnetic field with a field reversal time less than the material's magnetic relaxation time, both of these events take place.[159] **Figure 15** illustrates the

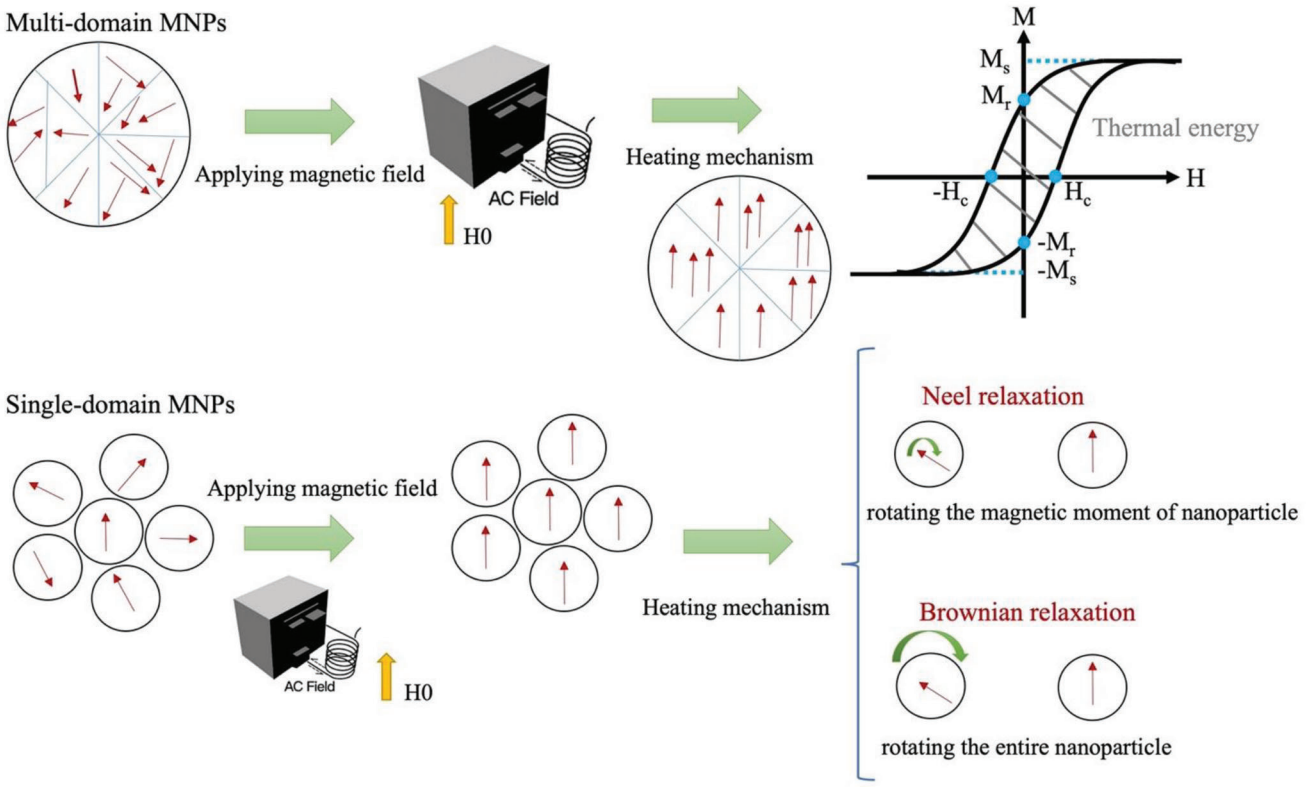

Figure 15. Heat generation mechanisms of hysteresis loss and Néel and Brownian relaxation.

three independent heat generation mechanisms in magnetic hyperthermia.

5.4. MNPs for Drug Delivery

The controlled release of drugs from nanostructured functional materials is becoming more and more attractive due to its potential for cancer therapy and other diseases.[167] A variety of materials with different structural shapes are being combined with medications to produce nanodrug delivery systems that can target specific areas of the body. Recent research has identified nanoparticles (including polymeric, ceramic, and metallic), liposomes, micelles, dendrimers, and carbon nanostructures as some of the most commonly used drug delivery vehicles[168] as shown in **Figure 16**.

In order to achieve the desired properties for drug delivery, it is important to carefully consider various factors of the system such as the nature, size, drug conjugation method (attached, adsorbed, encapsulated), surface chemistry/functionalization, hydrophilicity/hydrophobicity, biodegradability, and physical response properties (temperature, pH, electric charge, light, sound, magnetism). In this context, MNPs are of particular interest for therapeutic drug targeting. These particles can be systematically administered to a specific target in the human body guided by an external magnetic field, ultimately localizing them to the desired location.[175,176] Apart from their magnetic core properties, MNPs have the capacity to carry drugs and possess biochemical properties that can be improved by suitable coatings.[167] MNPs are effective drug delivery systems as they increase cellular absorption at targeted sites and decrease the in vivo distribution of cytotoxic agents. However, MNPs have a hydrophobic surface and a high surface-area-to-volume ratio, leading to cluster formation that increases the particle size and can cause embolization in the bloodstream, hindering blood flow. Cluster formation also affects the superparamagnetic properties of MNPs. Furthermore, when these particles reach the liver, they can induce a cytotoxicity.[176] To make MNPs compatible with therapeutic agents, their surface must be modified to enable effective loading and release of drugs at targeted sites. The most common methods for drug loading involve direct encapsulation or adsorption of drugs through physical interactions such as hydrophobic interactions or electrostatic attraction between MNPs and drug molecules. Alternatively, chemical reactions such as covalent bonding through active groups between the surface functional groups of MNPs and drug molecules can also be employed for drug loading.[177]

Magnetic drug delivery involves attaching or encapsulating therapeutic agents within MNPs. These particles can be composed of porous polymers with MNPs precipitated inside the pores, or they may have magnetic cores with polymer or metal coatings that can be functionalized. Through functionalization of the polymer or metal coating, it is possible to attach cytotoxic drugs for targeted chemotherapy or therapeutic DNA to correct a genetic defect.[178] Drug delivery systems based on the use of MNPs offer several benefits, including the ability to target specific locations in the body, the reduction of the amount of drug required to achieve a specific

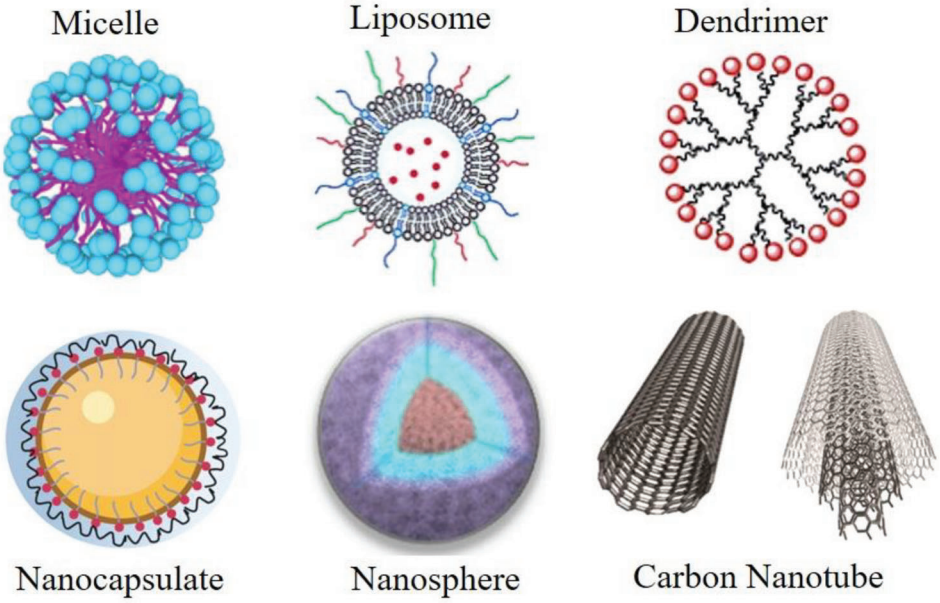

Figure 16. Different drug delivery vehicles. Micelle, Reproduced under the terms of the CC BY 4.0 license.[169] Copyright 2019. Liposome, Reproduced with permission.[170] Copyright 2019, American Chemical Society. Dendrimer, Reproduced with permission.[171] Copyright 2014, The Royal Society of Chemistry. Nanocapsulate, Reproduced with permission.[172] Copyright 2021, Controlled Release Society. Nanosphere, Reproduced under the terms of the CC BY 4.0 license.[173] Copyright 2019, Nature Research. Carbon nanotube, Reproduced with permission.[174] Copyright 2016, American Chemical Society.

concentration at the target site, and the prevention of serious side effects by decreasing the concentration of the drug at nontarget sites.[167]

Surface chemistry, size (magnetic core, hydrodynamic volume, and size distribution), and magnetic characteristics (magnetic moment, remanence, and coercivity) are key factors that determine the behavior of MNPs in drug delivery. To prevent the reticuloendothelial system (RES) from clearing MNPs and to extend their half-life in the bloodstream, it is essential to reduce particle size and modify surface chemistry by coating the MNPs with neutral and hydrophilic substances such as PEG, polysaccharides, and dysopsonins. However, complete avoidance of the RES is not always achievable, and migration to unintended parts of the body can cause toxicological issues. Therefore, the surfaces of MNPs are modified to promote robust bonding between biomolecules and nanoparticles. To deliver negatively charged drugs such as aspirin and ibuprofen, MNPs with a positively charged surface are used. Various anticancer drugs, enzymes, nonsteroidal anti-inflammatory drugs, folic acid, growth factors, mitomycin, and genes have been delivered to targeted cells using MNPs. MNPs and drugs are linked using linkers such as dextran, polystyrene, and silica. Once the MNPs–drug complexes reach the target site, drugs can be released into a medium containing negatively charged substances such as phosphate and chloride ions.[176]

In the study published by Pourjavadi et al., a novel class of multifunctional MNPs was synthesized. The TEM images of Fe_3O_4, Fe_3O_4@SiO_2, Fe_3O_4@SiO_2@PNG (PNG: poly(*N*-isopropyl acrylamide-*co*-glycidyl methacrylate)), and Fe_3O_4@SiO_2@PNG-Hy (Hy: hydrazine) MNPs are shown in **Figure 17**A. These MNPs exhibited dual temperature and pH responsive behavior and were intended to be used as a delivery system for the drug doxorubicin (DOX).[179] The research findings showed that the DOX release from DOX-loaded Fe_3O_4@SiO_2@PNG-Hy MNPs exhibited a good pH and temperature dependent release behavior (see Figure 17B). Furthermore, the MTT assay indicated that the DOX-loaded Fe_3O_4@SiO_2@PNG-Hy MNPs had remarkable cytotoxicity against cancer cells, while maintaining acceptable biocompatibility. Based on these results, the dual responsive nanocarriers are considered promising candidates for further investigations in cancer treatment.

In a different work, Ayubi et al. utilized PEGylated curcumin as the surface modification of MNPs (MNP@PEG-Cur) to take advantage of the magnetic targeting property of the nanoparticles and the PEG conjugated medication, as described in their research.[180] The TEM images showed that the synthesized MNPs were spherical (**Figure 18**A). The authors decorated the surface of the MNPs with curcumin by physically coupling it to the PEG hydroxyl functional groups. The results of a hemolysis assay (which holds great importance in gaining insight into the toxicity of samples in contact with human blood) demonstrated that all nanocarriers exhibited less than 5% hemolysis, thus showing a nonhemolytic response even at concentrations as high as 5 mg mL^{-1}. The MTT test results indicated that MNP@PEG-Cur was biocompatible and safe, with no toxicity detected up to a concentration of 100 µg mL^{-1}. Additionally, acute toxicity testing revealed a slight increase in the weight of mice after 24 h and one week after exposure, suggesting normal activity and behavior of all mice. The results of these tests illustrated the biocompatibility of MNP@PEG-Cur (see Figure 18B). The findings of the drug loading and release study demonstrated that, when comparing MNPs and free curcumin systems, the

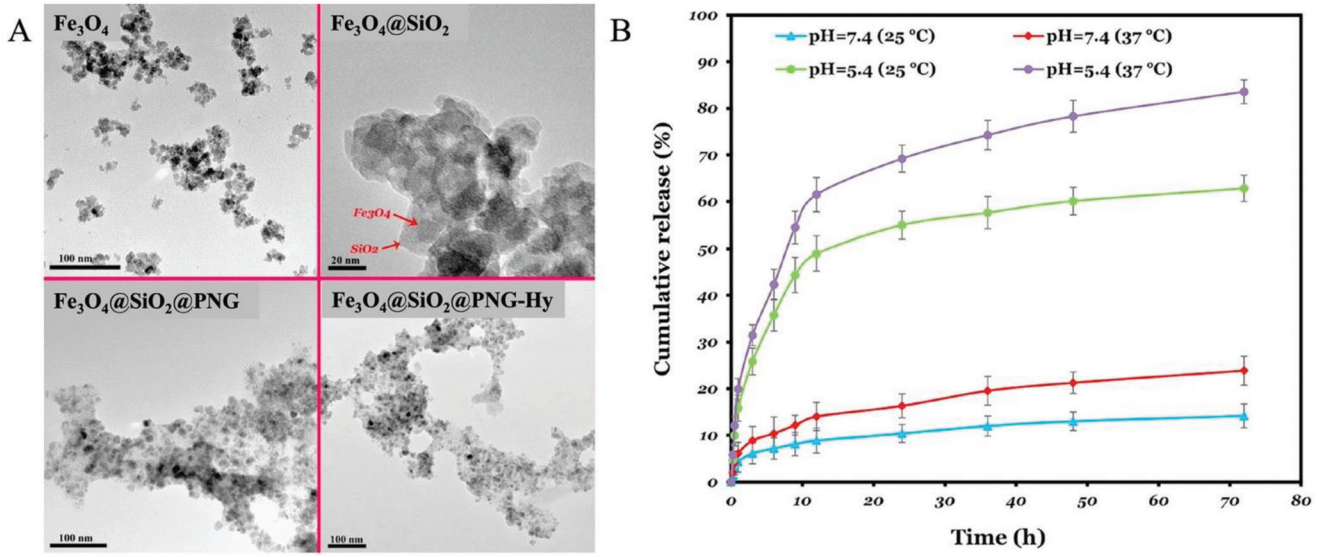

Figure 17. A) TEM images of MNPs with different coatings. B) In vitro cumulative DOX release profile of the pH- and thermosensitive nanocarrier Fe_3O_4@SiO_2@PNG-Hy. Reproduced with permission.[179] Copyright 2019, Elsevier B.V.

maximum concentration of the curcumin in the receiver was achieved with the particulate system, which suggests the higher solubility of curcumin in the nanoformulation. In addition, the nanoparticles exhibited a pH-sensitive release of curcumin, with a greater extent of drug release observed in acidic conditions. The maximum drug release achievable for MNP@PEG-Cur in both neutral and acidic media was 43.7% and 53.5%, respectively. These results can be attributed to the higher rate of curcumin–PEG linkage hydrolysis in the acidic environment and the improved solubility of curcumin in the acidic pH compared to the neutral pH (see Figure 18C).

5.5. MNPs for Magnetic Biosensors

Magnetic biosensors have received increasing attention due to their exceptional advantages over other types of biosensors.[181] One of the benefits of magnetic biosensors is their stability over time in cell culture, allowing for long-term labeling assays while fabricating tissues and organs. Unlike fluorescent tags, magnetic nanotags do not lose their integrity over time. In addition, magnetic materials do not produce background noise effects, which are common in fluorescently tagged samples due to the tissue's natural characteristics. Another advantage is the ability to monitor and control the biological environment from a distance by applying regulated magnetic fields from the exterior surface. Furthermore, magnetic assays have been shown to be more sensitive than fluorescence tests, allowing for detection at much lower protein concentrations.[182] Thus, one of the key benefits is the increased sensitivity, allowing for detection at lower concentrations of analytes. Additionally, the use of MNPs can result in a low limit of detection (LOD), a high signal-to-noise ratio, and faster analysis times, all of which are crucial in many applications such as clinical diagnosis and environmental monitoring.[183] In this area, MNPs have been extensively researched due to their inherent characteristics of magnetism and peroxidase activity. These properties are influenced by the size, shape, and surface chemistry of the particles. In bioassays, MNPs are beneficial in three ways: 1) they can be used for sample enrichment and separation based on their superparamagnetic behavior, 2) they can amplify signals due to their large surface area and mass, and high enzyme mimicking activity, and 3) they can be used for signal detection based on their magnetic, optical, or electrical properties.[181]

To enable biosensors, it is essential to immobilize biorecognition molecules such as enzymes, antibodies, and other biomolecules onto MNPs for target recognition. Different biorecognition mechanisms, including antibody–antigen interaction, aptamer recognition, and molecularly imprinted polymers, have been employed in biosensors. IO MNPs are commonly used as magnetic particles in biosensors due to their active surface, fast response kinetics, good chemical stability, and ease of surface modification. At the nanometer scale, these MNPs are responsive to magnetic fields and can disperse once the magnet is removed. With their potential for multiple uses and significant biosensor applications, MNPs are a promising material for future research.

5.5.1. MNPs for MPS-Based Biosensors

MPS is a technique that uses a search coil-based implementation to detect the nonlinear magnetization response of MNPs. This is shown in **Figure 19**B:B1. When a sinusoidal excitation field is applied, the nonlinear M–H curve of MNPs results in a nonlinear time-domain magnetization response that includes higher harmonics along with the base frequencies. This is illustrated in Figure 19A:A1,A:A2 for single- and dual-frequency excitation scenarios. MPS has been used for various applications, including thermometry,[68,184–187] and viscometry,[69,188–192] to bioassay implementations.[193–198] The idea of using MNPs for bioassay applications was first envisioned by Nikitin and Vetoshko in their

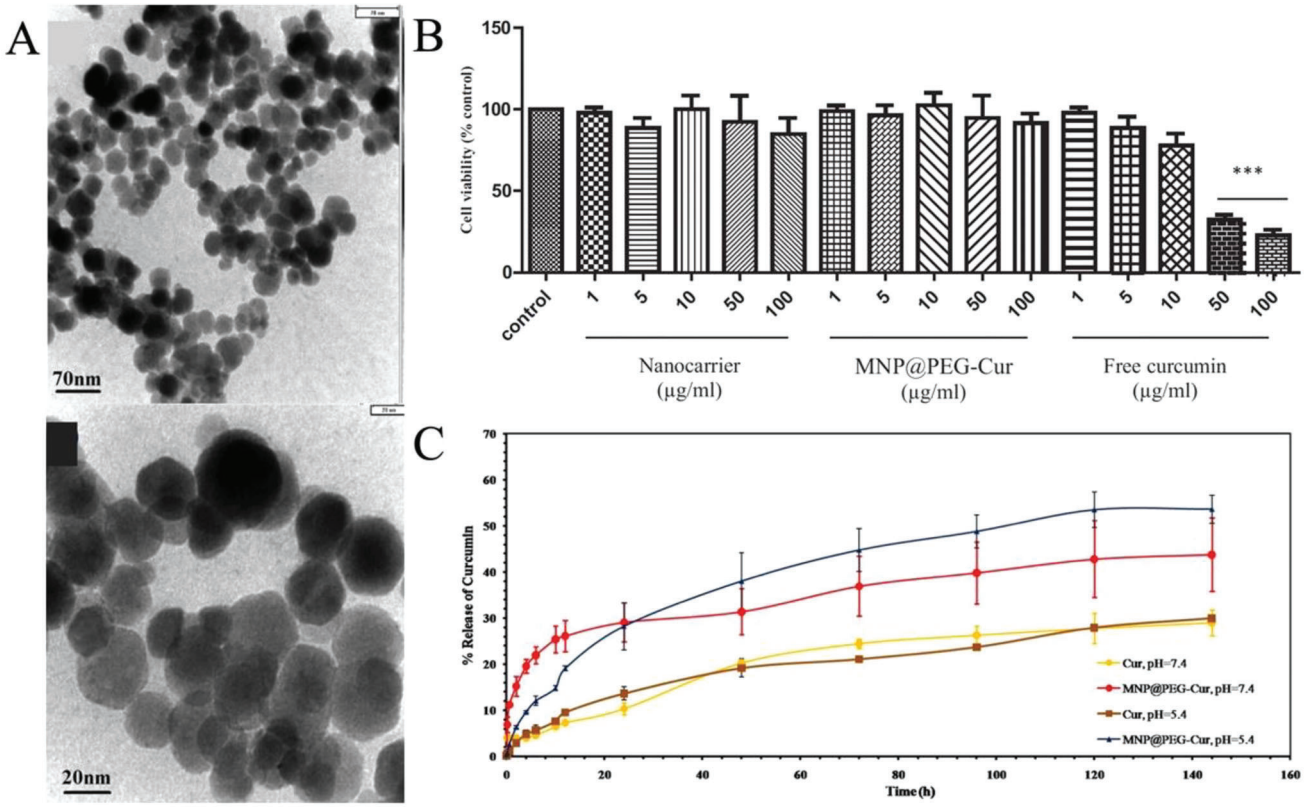

Figure 18. A) TEM analysis of MNP@PEG-Cur. B) Effect of MNP@PEG-Cur nanoparticles on viability of MCF7 cells. C) Drug release from MNP@PEG-Cur and curcumin at pH = 7.4, and pH = 5.4. Reproduced with permission.[180] Copyright 2019, Elsevier B.V.

2001 patent[199] and a dual-frequency based bioassay device was independently reported by Krause et al.[200] and Nikitin et al.[201] in 2007. There are two categories of MPS implementations: those that use a single-frequency excitation field and those that use a dual-frequency excitation field. Additionally, MPS-based bioassays are categorized based on the used MNP relaxation mechanism, with volumetric and surface-based assay implementations being the two main types.

Volumetric-MPS bioassays involve the use of MNPs dominated by Brownian relaxation for the detection of analytes. The Brownian relaxation of MNPs is influenced by factors such as the viscosity of the surrounding media (η), temperature (T), and the hydrodynamic size of the nanoparticles (V_H). As a result, the zero-field Brownian relaxation time can be expressed as[202,203]

$$\tau_B = \frac{3\eta V_H}{k_B T} \tag{4}$$

The zero-field Brownian relaxation time is calculated using the Boltzmann constant (k_B) and the previously mentioned parameters. In a bioassay designed for detecting a particular antigen, MNPs coated with the corresponding antibody are used. When the antigen is added to these MNPs, it leads to the formation of clusters, increasing the hydrodynamic size of the MNPs. This increase in this physical parameter causes a higher Brownian relaxation time and phase lag, which results in a reduction in the harmonic response of the MNPs. Figure 19B:B2 illustrates this volumetric bioassay process. The choice of the appropriate MNPs, excitation scenario (single- vs dual-frequency), and the corresponding field modulation parameters (frequency and amplitude of the applied excitation field) play a crucial role in determining the assay's performance.[204] Another crucial parameter for optimal clustering and thus, bioassay performance, is the relative concentration of MNPs and antigens. The sensitivity dependence on the MNP concentration for volumetric bioassays was first reported by Zhong et al.[205] for a single-frequency MPS system where an improvement in sensitivity was obtained with the utilization of lower MNP concentration. Later, Chugh et al.[206] reported a linear dependence between the sensitivity of dual-frequency MPS bioassays and the MNP concentration, i.e., a bioassay sensitivity improvement of a factor of 2, 4, and 8 was observed when using 2-, 4-, and 8-fold diluted MNPs, respectively, for the bioassay analysis.

Surface-based MPS bioassays depend on the Néel relaxation of MNPs. The zero-field Néel relaxation time is defined by:[207]

$$\tau_N = \frac{\sqrt{\pi}}{2\sqrt{\frac{KV}{k_B T}}} \frac{M_s\left(1+\alpha^2\right)}{2K\gamma\alpha} \exp\left(\frac{KV}{k_B T}\right) = \tau_0 \exp\left(\frac{KV}{k_B T}\right) \tag{5}$$

where K is the magnetic anisotropy constant, V is the MNP core volume, and α and γ represent the material-specific Gilbert damping coefficient and the gyromagnetic ratio of the electron, respectively. It can be noted that a change in the physical state of

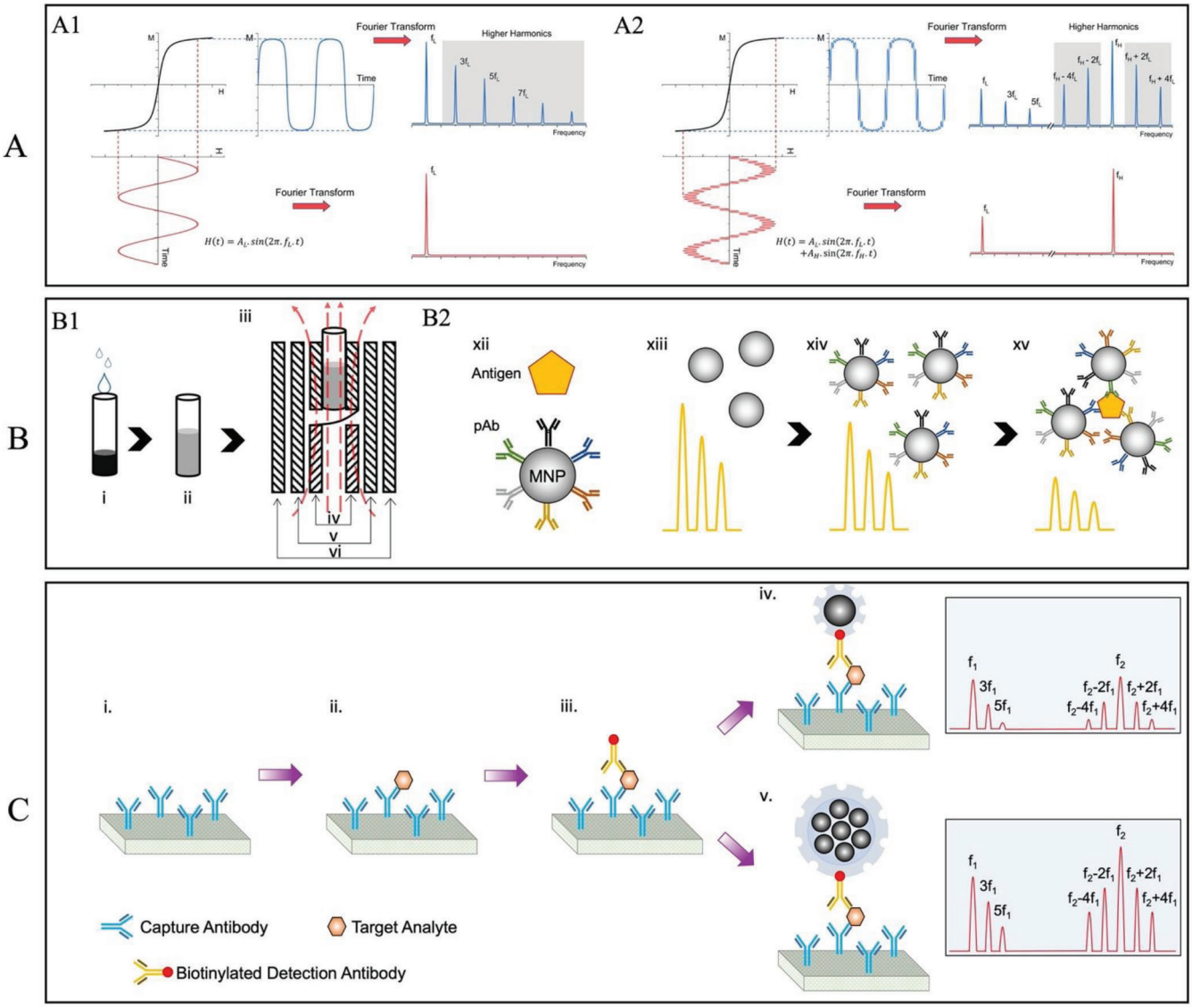

Figure 19. A) Magnetization response of superparamagnetic nanoparticles under the application of (A:A1) single and (A:A2) dual-excitation fields along with the higher harmonic decomposition after fast Fourier transform (FFT) implementation on the time-domain magnetization response. B) Schematic depiction of a dual-frequency volumetric MPS bioassay. (B:B1) Successive steps involved in a volumetric bioassay depicting fluidic sample addition and MPS readout. (B:B2) Changes in the harmonic spectra of MNPs resulting from cluster formation in volumetric MPS. C) Surface-based MPS bioassay implementation utilizing a sandwich assay mechanism. A) Reproduced with permission.[208] Copyright 2019, IOP Publishing Ltd. B) Reproduced with permission.[209] Copyright 2021, American Chemical Society. C) Reproduced with permission.[204] Copyright 2022, American Chemical Society.

the MNP does not cause any impact on the Néel relaxation time. Thus, surface-based MPS schemes utilize the sandwich bioassay technique to capture MNPs through antibody–antigen reactions to quantify the presence of an analyte. Figure 19C depicts a schematic view of this surface-based MPS bioassay. In this type of bioassay, the first step involves coating the reaction surface with capture antibodies that are specific to the target analyte. Next, a biofluidic sample is allowed to flow inside the system, leading to the conjugation of the analyte with the capture antibodies on the surface. Any excess analyte is then washed away through a washing step. Next, biotinylated detection antibodies are generally added to the surface, completing the sandwich bioassay step for the recognition of the target analyte. After, streptavidin-coated MNPs areinjected to magnetically tag the target analytes for the MPS readout. The MPS reading provides a harmonic readout that correlates with the presence of analytes in the test sample.

5.5.2. MNPs for Magnetoresistive (MR) Biosensors

Aside from the MPS-based biosensors, MNPs are also indispensable labels for MR biosensors. To date, MR biosensors have been developed based on three major MR effects, which are the anisotropic magnetoresistance (AMR),[210,211] giant magnetoresistance (GMR),[212,213] and tunneling magnetoresistance

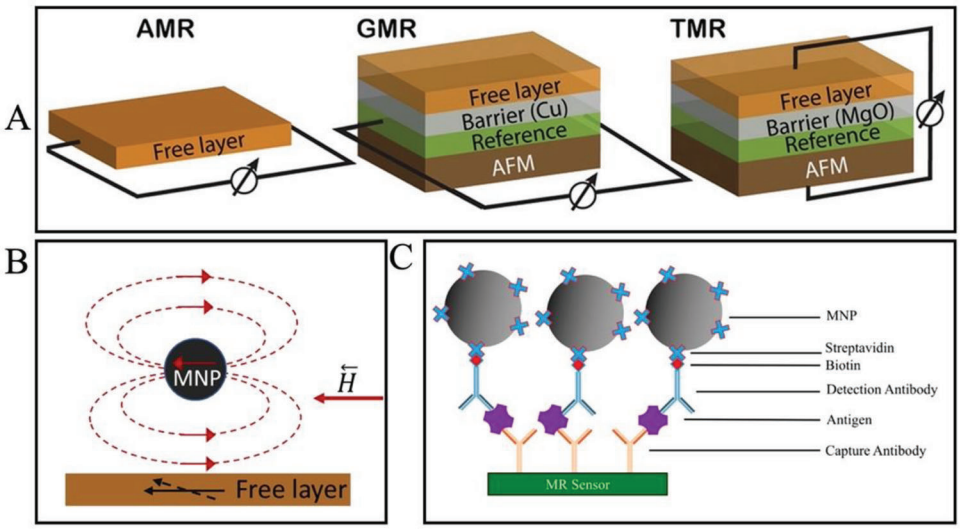

Figure 20. Schematic view of A) the general structures of AMR, GMR, and TMR sensors, B) Stray field generated by MNPs, C) MNP-based sandwich immunoassay. A) Reproduced under the terms of the CC BY 4.0 license.[216] Copyright 2020, Wiley-VCH. C) Reproduced under the terms of the CC BY 4.0 license.[227] Copyright 2019, MDPI.

(TMR).[214,215] Although the mechanisms underlying these three MR effects differ, they all refer to the change in the electrical resistance observed in response to an applied magnetic field in ferromagnetic material systems. The mathematical definition of magnetoresistance is expressed as the MR ratio, which is equal to the change in resistance (ΔR) divided by the reference resistance (R_0). Typically, the reference resistance is chosen as the lowest resistance that occurs within the given range of applied magnetic fields.

Figure 20A depicts the basic structures of these three MR sensors.[216] Among them, AMR sensors have the simplest structure with only one layer of ferromagnetic (FM) metals, usually Ni, Co, Fe, or their alloys.[217] The magnetization direction of the FM layer can rotate when subjected to an external magnetic field and is therefore called the free layer. In this structure, the electrical resistance varies as the angle between the applied current and the magnetization direction changes. Although AMR was the first discovered MR effect, the concept of developing MR biosensors was first proposed based on the GMR effect.[218]

The GMR effect was initially observed in alternating ferromagnetic/nonmagnetic metal (FM/NM) multilayer structures, but the spin–valve (SV) structure is the most studied GMR biosensor. The SV structure consists of a free layer and a reference layer made of ferromagnetic materials, with a nonmagnetic metal layer as a barrier between them. When an external magnetic field is applied, the magnetization direction of the free layer rotates, while the magnetization direction of the reference layer remains fixed due to the underlying antiferromagnetic layer. As the magnetization direction of the free layer rotates from being parallel to the reference layer to being antiparallel, the resistance of the entire structure increases. By replacing the barrier layer in a GMR SV sensor with a nonmagnetic insulator, the structure becomes a TMR sensor, also known as a magnetic tunnel junction (MTJ). The resistance in an MTJ reaches its maximum state when the magnetization directions of the two ferromagnetic layers are parallel, and its minimum state when the directions are antiparallel.

Despite the different mechanisms and geometries of the aforementioned MR sensors, the basic working principle for them being used as detection platforms is similar. As shown in Figure 20B, when an external magnetic field is applied, the MNPs located near the surface of an MR sensor generate a stray field, which in turn affects the magnetization of the free layer. The MR sensor experiences a change in the resistance as a result of this change in magnetization. The impact of stray fields generated by MNPs on MR sensors has been investigated using theoretical models, and the results have been compared with experimental findings.[219–222] In general, the strength of the stray field increases as the number of MNPs near the surface of the MR sensor increases. Consequently, the number of MNPs near the sensor surface can be quantified by the change on the MR ratio.

In order to determine the effectiveness of MR sensors in detecting biological analytes, it is important to establish a relationship between their ability to quantify MNPs and their practical utility. This is accomplished through the use of bioassays, such as protein or DNA assays, depending on the specific type of analyte being detected. An example of a commonly used bioassay is the sandwich immunoassay for antigen detection, which involves capturing MNPs on the surface of the sensor and measuring their stray field to establish a quantitative correlation between the MNPs and the target analytes. By measuring the change in the MR ratio of the sensor, which indicates the number of MNPs, it is possible to determine the number of target analytes present in the sample. Figure 20C provides a visual representation of this process.

Since detecting biological analytes using MR sensors involves essentially detecting MNP labels, the choice of the MNPs is critical. To ensure the effective utilization of MNPs in MR biosensors, two key parameters to be considered are the composition and the geometry of the MNPs. In terms of composition, the most used MNPs for MR biosensors are Fe_3O_4 for their stability and biocompatibility.[223] Yet the relatively low Ms of Fe_3O_4 MNPs inhibits further optimization of their biosensing abilities.

Therefore, high moment MNPs such as Fe and FeCo MNPs have been developed to improve the sensitivity and LOD of MR sensors.[224] For example, Srinivasan et al. reported a zeptomole (10^{-21} mol) detection sensitivity of a GMR sensor by using high-moment FeCo nanoparticles.[225] The influence of the MNPs geometry on the detection ability includes the particle size and shape. Increasing the size of the MNPs can lead to a higher magnetic moment. However, excessively large MNPs will lose their superparamagnetic properties, and their magnetic response will become more complex. Therefore, it is essential to strike a balance between maximizing the magnetic moment and ensuring that the MNPs remain in the superparamagnetic regime to achieve an optimal performance in MR biosensors.[15] As for the shape of the MNPs, although mostly used MNPs are spherical, recent research indicates that cubic MNPs may have better performance than nanospheres due to their stronger binding abilities and enhanced magnetic properties.[226]

6. Conclusions and Future Remarks

In this review, we have provided a thorough overview of the MNP design, synthesis, and functionalization, as well as the relevant biomedical applications of these materials since MNP research and development for biomedical applications have significantly increased in recent years. Indeed, there has been extensive research into prospective applications because of the MNPs' capacity to be synthesized with controlled size, monodispersity, shape, and surface functioning. Additionally, MNPs can be precisely targeted to a particular area of the body by using external magnetic fields, which makes them useful in multiple applications as therapeutic and diagnostic agents, as well as for imaging and drug delivery systems.

Various approaches, including physical, chemical, and biological, have been developed over the years for the reproducible production of high-quality MNPs. The ability to obtain small particles with precise control over their size, shape, and size distribution makes chemical synthesis (including coprecipitation, hydrothermal, sol–gel, microemulsion, thermal decomposition and microwave assisted synthesis) the most preferred methods for the MNP manufacture. However, most methods present several drawbacks as well that must be taken into consideration for the synthesis of MNPs employed in biomedical applications. Particularly, for the greatest outcomes in biological applications, reproducible synthetic processes are still needed for producing biocompatible formulations in a single step that are chemically stable, uniform in size, and effectively distributed in aqueous media with optimum surface coatings.

While significant progress has been done on magnetically induced hyperthermia, drug delivery, imaging, and biosensing applications, the translation of this research into clinical trials possesses significant challenges for future investigations. To successfully utilize MNPs in human applications, special attention and effort are required. Both in vitro (laboratory) and in vivo (animal) studies are necessary to assess the long-term stability and potential toxicity of MNPs. It is crucial to thoroughly understand how MNPs interact with human tissues and cells to ensure their safety and efficacy. Another obstacle to overcome is the ecotoxicity of certain nanoparticles. Some MNPs may have adverse effects on the environment and ecosystems, which must not be overlooked. Researchers need to address these concerns and develop strategies to minimize any potential harm. However, despite these challenges, we emphasize that further advancements in comprehensive studies can make the effective clinical application of MNPs a viable option soon. Continued research and development are essential to enhance our understanding of MNPs and maximize their potential benefits in medical applications.

Acknowledgements

This study was financially supported by the Texas Tech University through HEF New Faculty Startup, NRUF Start Up and Core Research Support Fund. B.R. acknowledges the Distinguished Graduate Student Assistantships (DGSA) offered by the Texas Tech University. V.K.C. acknowledges the Interdisciplinary Doctoral Fellowship (IDF) offered by the University of Minnesota.

Conflict of Interest

The authors declare no conflict of interest.

Keywords

biocompatibility, drug delivery, hyperthermia therapy, magnetic biosensors, magnetic imaging, magnetic nanoparticles

Received: June 8, 2023
Revised: August 24, 2023
Published online: September 21, 2023

[1] P. M. Martins, A. C. Lima, S. Ribeiro, S. Lanceros-Mendez, P. Martins, *ACS Appl. Bio Mater.* **2021**, *4*, 5839.
[2] A. A. Yaqoob, H. Ahmad, T. Parveen, A. Ahmad, M. Oves, I. M. I. Ismail, H. A. Qari, K. Umar, M. N. Mohamad Ibrahim, *Front. Chem.* **2020**, *8*, 341.
[3] H.-W. Zhang, Y. Liu, S.-H. Sun, *Front. Phys. China* **2010**, *5*, 347.
[4] N. A. Frey, S. Sun, in *Inorganic Nanoparticles: Synthesis, Application, and Perspective*, (Eds: C. Altavilla, E. Ciliberto), CRC Press, Boca Raton, **2010**, 33-68.
[5] C. Jiang, C. W. Leung, P. W. T. Pong, *Appl. Surf. Sci.* **2017**, *419*, 692.
[6] A. Weddemann, I. Ennen, A. Regtmeier, C. Albon, A. Wolff, K. Eckstädt, N. Mill, M. K.-H. Peter, J. Mattay, C. Plattner, N. Sewald, A. Hütten, *Beilstein J. Nanotechnol.* **2010**, *1*, 75.
[7] Q. Zhang, X. Yang, J. Guan, *ACS Appl. Nano Mater.* **2019**, *2*, 4681.
[8] J. Govan, Y. Gun'ko, *Nanomaterials* **2014**, *4*, 222.
[9] C. González-Fernández, J. Gómez-Pastora, E. Bringas, M. Zborowski, J. J. Chalmers, I. Ortiz, *Ind. Eng. Chem. Res.* **2021**, *60*, 16780.
[10] M. Vaseem, F. A. Ghaffar, M. F. Farooqui, A. Shamim, *Adv. Mater. Technol.* **2018**, *3*, 1700242.
[11] L. Mohammed, H. G. Gomaa, D. Ragab, J. Zhu, *Particuology* **2017**, *30*, 1.
[12] J. Gómez Pastora, E. Bringas Elizalde, I. Ortiz Uribe, **2016**.
[13] B. G. Krug, J. A. Asumadu, *IEEE Sens. J.* **2015**, *15*, 4174.
[14] K. Wu, D. Su, J. Liu, R. Saha, J.-P. Wang, *Nanotechnology* **2019**, *30*, 502003.
[15] K. Wu, R. Saha, D. Su, V. D. Krishna, J. Liu, M. C.-J. Cheeran, J.-P. Wang, *ACS Appl. Nano Mater.* **2020**, *3*, 9560.
[16] J. Gómez-Pastora, E. Bringas, M. Lázaro-Díez, J. Ramos-Vivas, I. Ortiz, in *Drug Delivery Systems* (Eds: P. Stroeve, M. Mahmoudi), World Scientific, Singapore, **2018**, pp. 207.

[17] D. Stanicki, L. V. Elst, R. N. Muller, S. Laurent, *Curr. Opin. Chem. Eng.* **2015**, *8*, 7.
[18] P. Yari, B. Rezaei, C. Dey, V. K. Chugh, N. V. R. K. Veerla, J.-P. Wang, K. Wu, *Sensors* **2023**, *23*, 4411.
[19] M. K. Satheeshkumar, E. R. Kumar, P. Indhumathi, Ch. Srinivas, M. Deepty, S. Sathiyaraj, N. Suriyanarayanan, D. L. Sastry, *Inorg. Chem. Commun.* **2020**, *111*, 107578.
[20] R. Ghosh Chaudhuri, S. Paria, *Chem. Rev.* **2012**, *112*, 2373.
[21] K. K. Kefeni, T. A. M. Msagati, T. T. Nkambule, B. B. Mamba, *Mater. Sci. Eng., C* **2020**, *107*, 110314.
[22] H. M. Zaki, S. H. Al-Heniti, A. Hashhash, *J. Magn. Magn. Mater.* **2016**, *401*, 1027.
[23] A. Soufi, H. Hajjaoui, R. Elmoubarki, M. Abdennouri, S. Qourzal, N. Barka, *Appl. Surf. Sci. Adv.* **2021**, *6*, 100145.
[24] T. F. Marinca, I. Chicinas, O. Isnard, *Ceram. Int.* **2013**, *39*, 4179.
[25] B. K. Sodipo, O. A. Noqta, A. A. Aziz, M. Katsikini, F. Pinakidou, E. C. Paloura, *J. Alloys Compd.* **2023**, *938*, 168558.
[26] F. L. Deepak, M. Bañobre-López, E. Carbó-Argibay, M. F. Cerqueira, Y. Piñeiro-Redondo, J. Rivas, C. M. Thompson, S. Kamali, C. Rodríguez-Abreu, K. Kovnir, Y. V. Kolen'ko, *J. Phys. Chem. C* **2015**, *119*, 11947.
[27] C. Barrera, A. Herrera, Y. Zayas, C. Rinaldi, *J. Magn. Magn. Mater.* **2009**, *321*, 1397.
[28] I. Sharifi, H. Shokrollahi, S. Amiri, *J. Magn. Magn. Mater.* **2012**, *324*, 903.
[29] B. Rezaei, A. Kermanpur, S. Labbaf, *J. Magn. Magn. Mater.* **2019**, *481*, 16.
[30] P. Pradhan, J. Giri, R. Banerjee, J. Bellare, D. Bahadur, *J. Magn. Magn. Mater.* **2007**, *311*, 208.
[31] T. Ruthradevi, J. Akbar, G. Suresh Kumar, A. Thamizhavel, G. A. Kumar, R. K. Vatsa, G. C. Dannangoda, K. S. Martirosyan, E. K. Girija, *J. Alloys Compd.* **2017**, *695*, 3211.
[32] S. Y. Srinivasan, K. M. Paknikar, D. Bodas, V. Gajbhiye, *Nanomedicine* **2018**, *13*, 1221.
[33] S. Amiri, H. Shokrollahi, *Mater. Sci. Eng., C* **2013**, *33*, 1.
[34] M. Khatami, H. Q. Alijani, I. Sharifi, *IET Nanobiotechnol.* **2018**, *12*, 879.
[35] F. Ludwig, C. Balceris, T. Viereck, O. Posth, U. Steinhoff, H. Gavilan, R. Costo, L. Zeng, E. Olsson, C. Jonasson, C. Johansson, *J. Magn. Magn. Mater.* **2017**, *427*, 19.
[36] M. Khatami, H. Alijani, M. Nejad, R. Varma, *Appl. Sci.* **2018**, *8*, 411.
[37] A. M. El-Toni, M. A. Habila, J. P. Labis, Z. A. Alothman, M. Alhoshan, A. A. Elzatahry, F. Zhang, *Nanoscale* **2016**, *8*, 2510.
[38] K. Wu, J. Liu, V. K. Chugh, S. Liang, R. Saha, V. D. Krishna, M. C. Cheeran, J.-P. Wang, *Nano Futures* **2022**, *6*, 022001.
[39] A. V. Nomoev, S. P. Bardakhanov, M. Schreiber, D. G. Bazarova, N. A. Romanov, B. B. Baldanov, B. R. Radnaev, V. V. Syzrantsev, *Beilstein J. Nanotechnol.* **2015**, *6*, 874.
[40] Q. Yue, Y. Zhang, C. Wang, X. Wang, Z. Sun, X.-F. Hou, D. Zhao, Y. Deng, *J. Mater. Chem. A* **2015**, *3*, 4586.
[41] H. Guo, J. Jin, Y. Chen, X. Liu, D. Zeng, L. Wang, D.-L. Peng, *Chem. Commun.* **2016**, *52*, 6918.
[42] W. Peng, Z. Zhang, M. Rong, M. Zhang, *Polymers* **2019**, *11*, 1832.
[43] S. Raj, G. Adilbish, J.-W. Lee, S. Manohar Majhi, B.- Chon, C.-H. Lee, S.-H. Jeon, Y.-T. Yu, *Ceram. Int.* **2014**, *40*, 13621.
[44] H. Xu, W. Wang, *Angew. Chem.* **2007**, *119*, 1511.
[45] G. L. Li, C. A. Tai, K. G. Neoh, E. T. Kang, X. Yang, *Polym. Chem.* **2011**, *2*, 1368.
[46] J. Ge, Q. Zhang, T. Zhang, Y. Yin, *Angew. Chem.* **2008**, *120*, 9056.
[47] Q. Guan, M. Wang, The 10th World Biomaterials Congress (WBC 2016), Montreal, Canada, 17-22 May, **2016**.
[48] Q. Li, C. W. Kartikowati, S. Horie, T. Ogi, T. Iwaki, K. Okuyama, *Sci. Rep.* **2017**, *7*, 9894.
[49] H. Sharifi Dehsari, V. Ksenofontov, A. Möller, G. Jakob, K. Asadi, *J. Phys. Chem. C* **2018**, *122*, 28292.
[50] R. Singh, R. Bhateria, *Environ. Geochem. Health* **2021**, *43*, 2459.
[51] S. E. Sandler, B. Fellows, O. T. Mefford, *Anal. Chem.* **2019**, *91*, 14159.
[52] L. E. Piedra Marin, *Construction of an Electromagnet for the Development of a Vibrating Sample Magnetometer*, Universidad de Investigación de Tecnología Experimental Yachay, Urcuqui, Ecuador, **2020**.
[53] B. Kirupakar, B. Vishwanath, M. P. Sree, D. Deenadayalan, *Int. J. Pharm.* **2016**, *4*, 227.
[54] S. Mourdikoudis, R. M. Pallares, N. T. K. Thanh, *Nanoscale* **2018**, *10*, 12871.
[55] K. Enpuku, T. Minotani, T. Gima, Y. Kuroki, Y. Itoh, M. Yamashita, Y. Katakura, S. Kuhara, *Jpn. J. Appl. Phys.* **1999**, *38*, L1102.
[56] A. B. Pandhare, R. P. Patil, S. D. Delekar, in *Advances in Metal Oxides and Their Composites for Emerging Applications*, Elsevier, Amsterdam, **2022**, Ch. 19, pp. 673.
[57] X.-F. Zhang, Z.-G. Liu, W. Shen, S. Gurunathan, *Int. J. Mol. Sci.* **2016**, *17*, 1534.
[58] M. M. Modena, B. Rühle, T. P. Burg, S. Wuttke, *Adv. Mater.* **2019**, *31*, 1901556.
[59] S. Dawadi, S. Katuwal, A. Gupta, U. Lamichhane, R. Thapa, S. Jaisi, G. Lamichhane, D. P. Bhattarai, N. Parajuli, *J. Nanomater.* **2021**, *2021*, 1.
[60] P.-C. Lin, S. Lin, P. C. Wang, R. Sridhar, *Biotechnol. Adv.* **2014**, *32*, 711.
[61] K. Akhtar, S. A. Khan, S. B. Khan, A. M. Asiri, *Handbook of Materials Characterization*, Springer, Berlin, **2018**, pp. 113.
[62] J. Lim, S. P. Yeap, H. X. Che, S. C. Low, *Nanoscale Res. Lett.* **2013**, *8*, 1.
[63] W. Sun, in *Atomic Force Microscopy in Molecular and Cell Biology*, Springer, Berlin, **2018**, pp. 1.
[64] P. Hinterdorfer, M. F. Garcia-Parajo, Y. F. Dufrêne, *Acc. Chem. Res.* **2012**, *45*, 327.
[65] D. Titus, E. J. J. Samuel, S. M. Roopan, in *Green Synthesis, Characterization and Applications of Nanoparticles*, Elsevier, Amsterdam, **2019**, pp. 303.
[66] N. Saadatkhah, A. Carillo Garcia, S. Ackermann, P. Leclerc, M. Latifi, S. Samih, G. S. Patience, J. Chaouki, *Can. J. Chem. Eng.* **2020**, *98*, 34.
[67] S. E. McNeil, *Characterization of Nanoparticles Intended for Drug Delivery*, Vol. *697*, Springer, Berlin, **2011**.
[68] J. Zhong, M. Schilling, F. Ludwig, *J. Phys. D: Appl. Phys.* **2017**, *51*, 015001.
[69] A. M. Rauwerdink, J. B. Weaver, *J. Magn. Magn. Mater.* **2010**, *322*, 609.
[70] V. K. Chugh, S. Liang, P. Yari, K. Wu, J.-P. Wang, *J. Phys. D: Appl. Phys.* **2023**, *56*, 315001.
[71] F. Ludwig, C. Balceris, C. Jonasson, C. Johansson, *IEEE Trans. Magn.* **2017**, *53*, 1.
[72] A. L. Elrefai, T. Sasayama, T. Yoshida, K. Enpuku, *IEEE Trans. Magn.* **2017**, *53*, 1.
[73] F. Ludwig, C. Balceris, C. Johansson, *IEEE Trans. Magn.* **2017**, *53*, 1.
[74] T. Z. G. De La Torre, A. Mezger, D. Herthnek, C. Johansson, P. Svedlindh, M. Nilsson, M. Strømme, *Biosens. Bioelectron.* **2011**, *29*, 195.
[75] F. Ludwig, A. Guillaume, M. Schilling, N. Frickel, A. M. Schmidt, *J. Appl. Phys.* **2010**, *108*, 033918.
[76] K. K. Narayanasamy, M. Cruz-Acuña, C. Rinaldi, J. Everett, J. Dobson, N. D. Telling, *J. Colloid Interface Sci.* **2018**, *532*, 536.
[77] R. Salam, A. Dimyati, M. Silalahi, *J. Phys.: Conf. Ser.* **2018**, *1091*, 012018.

[78] M. Gumustas, C. T. Sengel-Turk, A. Gumustas, S. A. Ozkan, B. Uslu, in *Multifunctional Systems for Combined Delivery, Biosensing and Diagnostics*, Elsevier, Amsterdam, **2017**, pp. 67.
[79] Y. Lin, M. Zhou, X. Tai, H. Li, X. Han, J. Yu, *Matter* **2021**, *4*, 2309.
[80] N. Ishida, V. S. J. Craig, *KONA* **2019**, *36*, 187.
[81] Y. Asakuma, T. Munenaga, R. Nakata, *Heat Mass Transfer* **2016**, *52*, 1833.
[82] I. F. Cruz, C. Freire, J. P. Araújo, C. Pereira, A. M. Pereira, in *Magnetic Nanostructured Materials*, Elsevier, New York, **2018**, pp. 59.
[83] L. Cabrera, S. Gutierrez, N. Menendez, M. P. Morales, P. Herrasti, *Electrochim. Acta* **2008**, *53*, 3436.
[84] N. Basavegowda, K.-H. Baek, *Molecules* **2021**, *26*, 912.
[85] A.-G. Niculescu, C. Chircov, A. M. Grumezescu, *Methods* **2022**, *199*, 16.
[86] L. B. De Mello, L. C. Varanda, F. A. Sigoli, I. O. Mazali, *J. Alloys Compd.* **2019**, *779*, 698.
[87] K. N. Koo, A. F. Ismail, M. H. D. Othman, N. Bidin, M. A Rahman, *Malays. J. Fundam. Appl. Sci.* **2019**, *15*, 23.
[88] W. M. Daoush, *J. Nanomed. Res.* **2017**, *5*, 00118.
[89] N. A. Yazid, Y. C. Joon, *AIP Conf. Proc.* **2019**, *2124*, 020019.
[90] T. Saragi, B. Depi, S. Butarbutar, B. Permana, *J. Phys.: Conf. Ser.* **2018**, *1013*, 012190.
[91] R. Massart, *IEEE Trans. Magn.* **1981**, *17*, 1247.
[92] M. S. Darwish, H. Kim, H. Lee, C. Ryu, J. Y. Lee, Y. Yoon, *Nanomaterials* **2019**, *9*, 1176.
[93] L. Shen, Y. Qiao, Y. Guo, S. Meng, G. Yang, M. Wu, J. Zhao, *Ceram. Int.* **2014**, *40*, 1519.
[94] M. R. Zamani Kouhpanji, B. J. H. Stadler, *Sensors* **2020**, *20*, 2554.
[95] A. Ali, H. Zafar, M. Zia, I. Ul Haq, A. R. Phull, J. S. Ali, A. Hussain, *Nanotechnol., Sci. Appl.* **2016**, *9*, 49.
[96] S. F. Hasany, I. Ahmed, J. Rajan, A. Rehman, *Nanosci. Nanotechnol.* **2012**, *2*, 148.
[97] J. Peng, M. Hojamberdiev, Y. Xu, B. Cao, J. Wang, H. Wu, *J. Magn. Magn. Mater.* **2011**, *323*, 133.
[98] M. Kermanian, M. Naghibi, S. Sadighian, *Heliyon* **2020**, *6*, 04928.
[99] D. Bokov, A. Turki Jalil, S. Chupradit, W. Suksatan, M. Javed Ansari, I. H. Shewael, G. H. Valiev, E. Kianfar, *Adv. Mater. Sci. Eng.* **2021**, *2021*, 1.
[100] J. Xu, H. Yang, W. Fu, K. Du, Y. Sui, J. Chen, Y.i Zeng, M. Li, G. Zou, *J. Magn. Magn. Mater.* **2007**, *309*, 307.
[101] N. Sanpo, J. Wang, C. C. Berndt, *J. Nano Res.* **2013**, *25*, 110.
[102] A. H. Monfared, A. Zamanian, M. Beygzadeh, I. Sharifi, M. Mozafari, *J. Alloys Compd.* **2017**, *693*, 1090.
[103] S. Belaïd, S. Laurent, M. Vermeersch, L. V. Elst, D. Perez-Morga, R. N. Muller, *Nanotechnology* **2013**, *24*, 055705.
[104] S. Majidi, F. Zeinali Sehrig, S. M. Farkhani, M. Soleymani Goloujeh, A. Akbarzadeh, *Artif. Cells, Nanomed., Biotechnol.* **2016**, *44*, 722.
[105] I. O. Perez De Berti, M. V. Cagnoli, G. Pecchi, J. L. Alessandrini, S. J. Stewart, J. F. Bengoa, S. G. Marchetti, *Nanotechnology* **2013**, *24*, 175601.
[106] V. Patsula, L. Kosinová, M. Lovric´, L. Ferhatovic Hamzic´, M. Rabyk, R. Konefal, A. Paruzel, M. Slouf, V. Herynek, S. k. Gajovic´, *ACS Appl. Mater. Interfaces* **2016**, *8*, 7238.
[107] V. Patsula, D. Horák, J. Kucka, H. Macková, V. Lobaz, P. Francová, V. Herynek, T. S. Heizer, P. Páral, L. Sefc, *Sci. Rep.* **2019**, *9*, 10765.
[108] M. Eslamian, M. Shekarriz, *Recent Pat. Nanotechnol.* **2009**, *3*, 99.
[109] J. N. Solanki, Z. V. P. Murthy, *Ind. Eng. Chem. Res.* **2011**, *50*, 12311.
[110] A. K. Ganguli, A. Ganguly, S. Vaidya, *Chem. Soc. Rev.* **2010**, *39*, 474.
[111] M. A. Al-Kinani, A. J. Haider, S. Al-Musawi, *IOP Conf. Ser.: Mater. Sci. Eng.* **2020**, *987*, 012013.
[112] D. C. Onwudiwe, *Heliyon* **2019**, *5*, 01413.
[113] M. I. Anik, M. K. Hossain, I. Hossain, A. M. U. B. Mahfuz, M. T. Rahman, I. Ahmed, *Nano Sel.* **2021**, *2*, 1146.
[114] M. E. F. Brollo, S. Veintemillas-Verdaguer, C. M. Salván, M. d. P. Morales, *Contrast Media Mol. Imaging* **2017**, *2017*.
[115] S. A. Khan, in *Metal Nanoparticles for Drug Delivery and Diagnostic Applications*, Elsevier, New York, **2020**, pp. 1.
[116] D.-W. Lee, H. Fatima, K.-S. Kim, *J. Nanosci. Nanotechnol.* **2018**, *18*, 1414.
[117] W.-Y. Rho, H.-M. Kim, S. Kyeong, Y.-L. Kang, D.-H. Kim, H. Kang, C. Jeong, D.-E. Kim, Y.-S. Lee, B.-H. Jun, *J. Ind. Eng. Chem.* **2014**, *20*, 2646.
[118] A. Guerrero-Martínez, J. Pérez-Juste, L. M. Liz-Marzán, *Adv. Mater.* **2010**, *22*, 1182.
[119] X. Chu, J. Yu, Y.-L. Hou, *Chin. Phys. B* **2015**, *24*, 014704.
[120] A. K. Gupta, M. Gupta, *Biomaterials* **2005**, *26*, 3995.
[121] D. Chandra Sekhar, B. S. Diwakar, N. Madhavi, *Int. J. Nanosci. Nanotechnol.* **2020**, *16*, 209.
[122] E. Umut, *Mod. Surf. Eng. Treat.* **2013**, *20*, 185.
[123] E. Nassireslami, M. Ajdarzade, *Adv. Pharm. Bull.* **2018**, *8*, 201.
[124] G. S. Demirer, A. C. Okur, S. Kizilel, *J. Mater. Chem. B* **2015**, *3*, 7831.
[125] P. Yari, H. Farmani, A. Farmani, *Plasmonics* **2022**, *17*, 305.
[126] S. Moraes Silva, R. Tavallaie, L. Sandiford, R. D. Tilley, J. J. Gooding, *Chem. Commun.* **2016**, *52*, 7528.
[127] M. Bilal, H. M. N. Iqbal, S. F. Adil, M. R. Shaik, A. Abdelgawad, M. R. Hatshan, M. Khan, *J. Adv. Res.* **2022**, *38*, 157.
[128] E. Illés, E. Tombácz, M. Szekeres, I. Y. Tóth, Á. Szabó, B. Iván, *J. Magn. Magn. Mater.* **2015**, *380*, 132.
[129] A. M. Predescu, E. Matei, A. C. Berbecaru, C. Pantilimon, C. Dragan, R. Vidu, C. Predescu, V. Kuncser, *R. Soc. Open Sci.* **2018**, *5*, 171525.
[130] N. S. Remya, S. Syama, A. Sabareeswaran, P. V. Mohanan, *Int. J. Pharm.* **2016**, *511*, 586.
[131] R. P. Dhavale, R. P. Dhavale, S. C. Sahoo, P. Kollu, S. U. Jadhav, P. S. Patil, T. D. Dongale, A. D. Chougale, P. B. Patil, *J. Phys. Chem. Solids* **2021**, *148*, 109749.
[132] X. N. Pham, T. P. Nguyen, T. N. Pham, T. T. N. Tran, T. V. T. Tran, *Adv. Nat. Sci.: Nanosci. Nanotechnol.* **2016**, *7*, 045010.
[133] X.-H. Pham, E. Hahm, H.-M. Kim, B. S. Son, A. Jo, J. An, T. A. Tran Thi, D. Q. Nguyen, B.-H. Jun, *Nanomaterials* **2020**, *10*, 117.
[134] M. Riskin, B. Basnar, Y. Huang, I. Willner, *Adv. Mater.* **2007**, *19*, 2691.
[135] G. Antarnusa, E. Suharyadi, *Mater. Res. Express* **2020**, *7*, 056103.
[136] K. Chatterjee, S. Sarkar, K. Jagajjanani Rao, S. Paria, *Adv. Colloid Interface Sci.* **2014**, *209*, 8.
[137] L. Trahms, *Colloidal Magnetic Fluids: Basics, Development and Application of Ferrofluids*, Springer, Berlin, **2009**, pp. 327.
[138] H. Shokrollahi, *Mater. Sci. Eng., C* **2013**, *33*, 4485.
[139] M. B. Gawande, A. Goswami, T. Asefa, H. Guo, A. V. Biradar, D.-L. Peng, R. Zboril, R. S. Varma, *Chem. Soc. Rev.* **2015**, *44*, 7540.
[140] G.-P. Yan, L. Robinson, P. Hogg, *Radiography* **2007**, *13*, 5.
[141] M. Pernia Leal, S. Rivera-Fernández, J. M. Franco, D. Pozo, J. M. De La Fuente, M. L. García-Martín, *Nanoscale* **2015**, *7*, 2050.
[142] N. Lee, T. Hyeon, *Chem. Soc. Rev.* **2012**, *41*, 2575.
[143] J. Wan, X. Jiang, H. Li, K. Chen, *J. Mater. Chem.* **2012**, *22*, 13500.
[144] D. Pan, S. D. Caruthers, A. Senpan, A. H. Schmieder, S. A. Wickline, G. M. Lanza, *Wiley Interdiscip. Rev.: Nanomed. Nanobiotechnol.* **2011**, *3*, 162.
[145] D. Pan, A. H. Schmieder, S. A. Wickline, G. M. Lanza, *Tetrahedron* **2011**, *67*, 8431.
[146] E.-K. Lim, B. Kang, Y. Choi, E. Jang, S. Han, K. Lee, J.-S. Suh, S. Haam, Y.-M. Huh, *Nanotechnology* **2014**, *25*, 245103.
[147] Y.-D. Xiao, R. Paudel, J. Liu, C. Ma, Z.-S. Zhang, S.-K. Zhou, *Int. J. Mol. Med.* **2016**, *38*, 1319.
[148] R. G. D. Andrade, S. R. S. Veloso, E. M. S. Castanheira, *Int. J. Mol. Sci.* **2020**, *21*, 2455.

[149] Z. Mohammadi, N. Attaran, A. Sazgarnia, S. A. M. Shaegh, A. Montazerabadi, *IET Nanobiotechnol.* **2020**, *14*, 396.
[150] C. Billings, M. Langley, G. Warrington, F. Mashali, J. A. Johnson, *Int. J. Mol. Sci.* **2021**, *22*, 7651.
[151] B. Gleich, J. Weizenecker, *Nature* **2005**, *435*, 1214.
[152] C. Sun, J. S. H. Lee, M. Zhang, *Adv. Drug Delivery Rev.* **2008**, *60*, 1252.
[153] P. Vogel, J. Markert, M. A. Rückert, S. Herz, B. Keßler, K. Dremel, D. Althoff, M. Weber, T. M. Buzug, T. A. Bley, *Sci. Rep.* **2019**, *9*, 1.
[154] E. U. Saritas, P. W. Goodwill, L. R. Croft, J. J. Konkle, K. Lu, B.o Zheng, S. M. Conolly, *J. Magn. Reson.* **2013**, *229*, 116.
[155] T. Knopp, T. M. Buzug, *Magnetic Particle Imaging: An Introduction to Imaging Principles and Scanner Instrumentation*, Springer Science & Business Media, Berlin, **2012**.
[156] A. Weber, F. Werner, J. Weizenecker, T. M. Buzug, T. Knopp, *Phys. Med. Biol.* **2015**, *61*, 475.
[157] Y. Du, X. Liu, Q. Liang, X.-J. Liang, J. Tian, *Nano Lett.* **2019**, *19*, 3618.
[158] Z. Nemati, J. Alonso, H. Khurshid, M. H. Phan, H. Srikanth, *RSC Adv.* **2016**, *6*, 38697.
[159] J. Jose, R. Kumar, S. Harilal, G. E. Mathew, D. G. T. Parambi, A. Prabhu, M.d. S. Uddin, L. Aleya, H. Kim, B. Mathew, *Environ. Sci. Pollut. Res.* **2020**, *27*, 19214.
[160] M. Bañobre-López, A. Teijeiro, J. Rivas, *Rep. Pract. Oncol. Radiother.* **2013**, *18*, 397.
[161] I. Hilger, *Int. J. Hyperthermia* **2013**, *29*, 828.
[162] A. E. Deatsch, B. A. Evans, *J. Magn. Magn. Mater.* **2014**, *354*, 163.
[163] Z. Hedayatnasab, F. Abnisa, W. M. A. W. Daud, *Mater. Des.* **2017**, *123*, 174.
[164] Z. Kamal, J. Su, M. Qiu, in *Metal Nanoparticles for Drug Delivery and Diagnostic Applications*, Elsevier, New York, **2020**, pp. 13.
[165] K. M. Krishnan, A. B. Pakhomov, Y. Bao, P. Blomqvist, Y. Chun, M. Gonzales, K. Griffin, X. Ji, B. K. Roberts, *J. Mater. Sci.* **2006**, *41*, 793.
[166] J.-P. Fortin, F. Gazeau, C. Wilhelm, *Eur. Biophys. J.* **2008**, *37*, 223.
[167] J. Dobson, *Drug Dev. Res.* **2006**, *67*, 55.
[168] A. P. Singh, A. Biswas, A. Shukla, P. Maiti, *Signal Transduction Targeted Ther.* **2019**, *4*, 33.
[169] W.-J. Wang, Y.-C. Huang, C.-M. Su, T.-R. Ger, *Front. Chem.* **2019**, *7*, 93.
[170] Y. Mo, H. Du, B. Chen, D. Liu, Q. Yin, Y. Yan, Z. Wang, F. Wan, T. Qi, Y. Wang, *ACS Biomater. Sci. Eng.* **2019**, *5*, 2316.
[171] A.-M. Caminade, C.-O. Turrin, *J. Mater. Chem. B* **2014**, *2*, 4055.
[172] M. Plaza-Oliver, M. J. Santander-Ortega, M. V. Lozano, *Drug Delivery Transl. Res.* **2021**, *11*, 471.
[173] B. Fortuni, T. Inose, M. Ricci, Y. Fujita, I. Van Zundert, A. Masuhara, E. Fron, H. Mizuno, L. Latterini, S. Rocha, H. Uji-I, *Sci. Rep.* **2019**, *9*, 2666.
[174] R. Alshehri, A. M. Ilyas, A. Hasan, A. Arnaout, F. Ahmed, A. Memic, *J. Med. Chem.* **2016**, *59*, 8149.
[175] V. V. Mody, A. Cox, S. Shah, A. Singh, W. Bevins, H. Parihar, *Appl. Nanosci.* **2014**, *4*, 385.
[176] A. Shah, S. Aftab, J. Nisar, M. N. Ashiq, F. J. Iftikhar, *J. Drug Delivery Sci. Technol.* **2021**, *62*, 102426.
[177] J. Huang, Y. Li, A. Orza, Q. Lu, P. Guo, L. Wang, L. Yang, H. Mao, *Adv. Funct. Mater.* **2016**, *26*, 3818.
[178] S. C. McBain, H. H. Yiu, J. Dobson, *Int. J. Nanomed.* **2008**, *3*, 169.
[179] A. Pourjavadi, M. Kohestanian, C. Streb, *Mater. Sci. Eng., C* **2020**, *108*, 110418.
[180] M. Ayubi, M. Karimi, S. Abdpour, K. Rostamizadeh, M. Parsa, M. Zamani, A. Saedi, *Mater. Sci. Eng., C* **2019**, *104*, 109810.
[181] Y. Xianyu, Q. Wang, Y. Chen, *TrAC, Trends Anal. Chem.* **2018**, *106*, 213.
[182] V. Nabaei, R. Chandrawati, H. Heidari, *Biosens. Bioelectron.* **2018**, *103*, 69.
[183] T. A. P. Rocha-Santos, *TrAC, Trends Anal. Chem.* **2014**, *62*, 28.
[184] T. Q. Bui, W. L. Tew, S. I. Woods, *J. Appl. Phys.* **2020**, *128*, 224901.
[185] J. B. Weaver, A. M. Rauwerdink, E. W. Hansen, *Med. Phys.* **2009**, *36*, 1822.
[186] Z. Du, Y.i Sun, O. Higashi, Y. Noguchi, K. Enpuku, S. Draack, K.-J. Janssen, T. Kahmann, J. Zhong, T. Viereck, F. Ludwig, T. Yoshida, *Jpn. J. Appl. Phys.* **2019**, *59*, 010904.
[187] I. Perreard, D. Reeves, X. Zhang, E. Kuehlert, E. Forauer, J. Weaver, *Phys. Med. Biol.* **2014**, *59*, 1109.
[188] K. Wu, J. Liu, Y.i Wang, C. Ye, Y. Feng, J.-P. Wang, *Appl. Phys. Lett.* **2015**, *107*, 053701.
[189] K. Wu, C. Ye, J. Liu, Y. Wang, Y. Feng, J.-P. Wang, *IEEE Trans. Magn.* **2016**, *52*, 1.
[190] J. B. Weaver, M. Harding, A. M. Rauwerdink, E. W. I. Hansen, *Proc. SPIE* **2010**, *7626*, 655.
[191] T. Yoshida, T. Nakamura, O. Higashi, K. Enpuku, *J. Magn. Magn. Mater.* **2019**, *471*, 334.
[192] A. L. Elrefai, T. Yoshida, K. Enpuku, *J. Magn. Magn. Mater.* **2020**, *507*, 166809.
[193] S. Achtsnicht, C. Neuendorf, T. Faßbender, G. Nölke, A. Offenhäusser, H.-J. Krause, F. Schröper, *PLoS One* **2019**, *14*, 0219356.
[194] S. Achtsnicht, J. Tödter, J. Niehues, M. Telöken, A. Offenhäusser, H.-J. Krause, F. Schröper, *Sensors* **2019**, *19*, 148.
[195] J. Pietschmann, D. Dittmann, H. Spiegel, H.-J. Krause, F. Schröper, *Foods* **2020**, *9*, 1773.
[196] J. Pietschmann, N. Voepel, L. Voß, S. Rasche, M. Schubert, M. Kleines, H.-J. Krause, T. M. Shaw, H. Spiegel, F. Schroeper, *Front. Microbiol.* **2021**, *12*, 643275.
[197] A. Rabehi, B. Garlan, S. Achtsnicht, H.-J. Krause, A. Offenhäusser, K. Ngo, S. Neveu, S. Graff-Dubois, H. Kokabi, *Sensors* **2018**, *18*, 1747.
[198] S. Achtsnicht, A. M. Pourshahidi, A. Offenhäusser, H.-J. Krause, *Sensors* **2019**, *19*, 2599.
[199] P. I. Nikitin, P. M. Vetoshko, Google Patent, US Patent 7,785,902, **2010**.
[200] H.-J. Krause, N. Wolters, Y. Zhang, A. Offenhäusser, P. Miethe, M. H. F. Meyer, M. Hartmann, M. Keusgen, *J. Magn. Magn. Mater.* **2007**, *311*, 436.
[201] P. I. Nikitin, P. M. Vetoshko, T. I. Ksenevich, *J. Magn. Magn. Mater.* **2007**, *311*, 445.
[202] N. V. Brilliantov, V. P. Denisov, P. L. Krapivsky, *Phys. A* **1991**, *175*, 293.
[203] D. A. Turton, K. Wynne, *J. Phys. Chem. B* **2014**, *118*, 4600.
[204] V. K. Chugh, A. di Girolamo, V. D. Krishna, K. Wu, M. C. Cheeran, J.-P. Wang, *J. Phys. Chem. C* **2023**, *127*, 450.
[205] J. Zhong, K.-J. Janssen, S. Draack, T. Viereck, M. Schilling, F. Ludwig, *J. Magn. Magn. Mater.* **2021**, *517*, 167408.
[206] V. K. Chugh, K. Wu, V. D. Krishna, A. Di Girolamo, R. P. Bloom, Y. A. Wang, R. Saha, S. Liang, M. C.-J. Cheeran, J.-P. Wang, *J. Phys. Chem. C* **2021**, *125*, 17221.
[207] S. Draack, N. Lucht, H. Remmer, M. Martens, B. Fischer, M. Schilling, F. Ludwig, T. Viereck, *J. Phys. Chem. C* **2019**, *123*, 6787.
[208] K. Wu, D. Su, R. Saha, D. Wong, J.-P. Wang, *J. Phys. D: Appl. Phys.* **2019**, *52*, 173001.
[209] K. Wu, V. K. Chugh, A. Di Girolamo, J. Liu, R. Saha, D. Su, V. D. Krishna, A. Nair, W. Davies, Y. A. Wang, *ACS Appl. Mater. Interfaces* **2021**, *13*, 7966.
[210] L. K. Quynh, B. D. Tu, C. V. Anh, N. H. Duc, A. T. Phung, T. T. Dung, D. T. H. Giang, *J. Electron. Mater.* **2019**, *48*, 997.
[211] M. M. Miller, G. A. Prinz, S.-F. Cheng, S. Bounnak, *Appl. Phys. Lett.* **2002**, *81*, 2211.
[212] K. Wu, T. Klein, V. D. Krishna, D. Su, A. M. Perez, J.-P. Wang, *ACS Sens.* **2017**, *2*, 1594.

[213] J. Choi, A. W. Gani, D. J. B. Bechstein, J.-R. Lee, P. J. Utz, S. X. Wang, *Biosens. Bioelectron.* **2016**, *85*, 1.
[214] L. Lei, T. Carvajal, M. Koslowski, *J. Appl. Phys.* **2012**, *111*, 07E505.
[215] Y. Wu, Y. Liu, Q. Zhan, J. P. Liu, R.-W. Li, *AIP Adv.* **2017**, *7*, 056658.
[216] S. Zuo, H. Heidari, D. Farina, K. Nazarpour, *Adv. Mater. Technol.* **2020**, *5*, 2000185.
[217] T. Mcguire, R. Potter, *IEEE Trans. Magn.* **1975**, *11*, 1018.
[218] D. R. Baselt, G. U. Lee, M. Natesan, S. W. Metzger, P. E. Sheehan, R. J. Colton, *Biosens. Bioelectron.* **1998**, *13*, 731.
[219] J. C. Rife, M. M. Miller, P. E. Sheehan, C. R. Tamanaha, M. Tondra, L. J. Whitman, *Sens. Actuators, A* **2003**, *107*, 209.
[220] H. A. Ferreira, D. L. Graham, P. P. Freitas, J. M. S. Cabral, *J. Appl. Phys.* **2003**, *93*, 7281.
[221] M. Tondra, M. Porter, R. J. Lipert, *J. Vac. Sci. Technol., A* **2000**, *18*, 1125.
[222] C. D. Damsgaard, M. F. Hansen, *J. Appl. Phys.* **2008**, *103*, 064512.
[223] Y. Jing, S.-H. He, J.-P. Wang, *IEEE Trans. Magn.* **2012**, *49*, 197.
[224] J. Liu, D. Su, K. Wu, J.-P. Wang, *J. Nanopart. Res.* **2020**, *22*, 66.
[225] B. Srinivasan, Y. Li, Y. Jing, Y. Xu, X. Yao, C. Xing, J.-P. Wang, *Angew. Chem., Int. Ed.* **2009**, *48*, 2764.
[226] A. G. Kolhatkar, Y.-T. Chen, P. Chinwangso, I. Nekrashevich, G. C. Dannangoda, A. Singh, A. C. Jamison, O. Zenasni, I. A. Rusakova, K. S. Martirosyan, D. Litvinov, S. Xu, R. C. Willson, T. R. Lee, *ACS Omega* **2017**, *2*, 8010.
[227] D. Su, K. Wu, R. Saha, C. Peng, J.-P. Wang, *Micromachines* **2019**, *11*, 34.

Bahareh Rezaei attained her M.Sc. in Materials Engineering from Isfahan University of Technology, Iran (2018). Currently, she is a Ph.D. candidate at Texas Tech University, also serving as a research assistant in the Department of Electrical and Computer Engineering. Her scholarly pursuits center on the synthesis and characterization of magnetic nanoparticles for biomedical purposes, encompassing magnetic particle imaging (MPI), magnetic resonance imaging (MRI) contrast agents, and hyperthermia treatment for cancer.

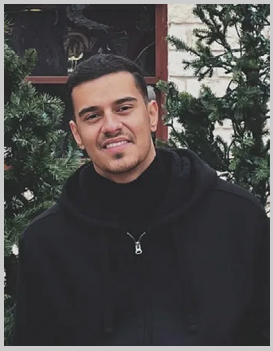

Parsa Yari obtained his B.Sc. from Razi University, Iran, and his M.Sc. from Texas Tech University, both within the discipline of Electrical Engineering. Currently engaged in his Ph.D. pursuit at Texas Tech University, his proficiency encompasses diverse domains including system design, magnetic particle imaging (MPI), electromagnetics, and plasmonic sensors.

Sean M. Sanders earned his Bachelor's degree in Chemical Engineering from Texas Tech University. His scholarly endeavors are dedicated to the chemical synthesis of magnetic nanoparticles. Presently, he holds the role of Chemical Engineer at Southwest Research Institute in San Antonio, Texas, where he continues to contribute to scientific advancements.

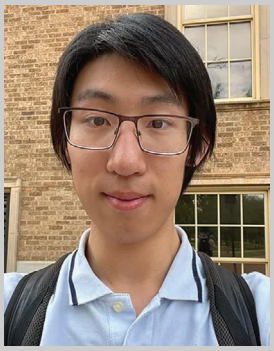

Haotong Wang is a third-year undergraduate enrolled in the Department of Chemical Engineering at Texas Tech University. He is deeply immersed in research centered on the chemical synthesis of magnetic nanoparticles.

Vinit Kumar Chugh completed his B.Tech. in Electrical Engineering at the Indian Institute of Technology Kharagpur in 2017. Subsequently, he garnered valuable experience in the semiconductor industry during 2017–2019, prior to embarking on his doctoral journey at the University of Minnesota in 2019. His scholarly pursuits revolve around magnetic sensors, biomedical systems, and their progressive applications, showcasing his commitment to pioneering research and innovation.

Shuang Liang graduated with a Bachelor's degree from Northwestern Polytechnical University and obtained her Master's degree from Northwestern University. Presently, she is a Ph.D. candidate at the University of Minnesota. Her research is predominantly focused on advancing magnetoresistance (MR)-based biosensors, aimed at the precise detection of biomarkers, showcasing her commitment to cutting-edge research in the field.

Shahriar Mostufa is presently pursuing a Ph.D. in the Electrical and Computer Engineering Department at Texas Tech University. He attained a Bachelor of Science (B.Sc.) degree in Electrical and Electronic Engineering from Rajshahi University of Engineering and Technology (RUET), Bangladesh, in 2022. His ongoing research endeavors encompass dynamic domains including metamaterials, nanophotonics, optical and magnetic biosensors, magnetic particle imaging, wearable electronics, and spintronics devices, affirming his engagement with cutting-edge advancements in multiple disciplines.

Kanglin Xu is a computer science undergraduate student with research focusing on machine learning algorithms and cybersecurity. He specializes in data analysis and visualization, extracting valuable insights from complex information. Beyond academia, Kanglin works as an information security technician, further fortifying his expertise in safeguarding digital realms.

Jian-Ping Wang is a fellow of IEEE, American Physical Society, and the National Academy of Inventors. He received his B.S. and M.S. degrees in Physics from Lanzhou University, Lanzhou in 1989 and 1992, respectively. He earned his B.S. and M.S. in Physics from Lanzhou University in 1989 and 1992, followed by a Ph.D. from the Institute of Physics, CAS, Beijing in 1995. He led the research department on magnetic materials and recording media as the technical manager at Data Storage Institute, Singapore (1998–2002). He joined the University of Minnesota in 2002 as an associate professor and is now a Distinguished McKnight University Professor and Robert F. Hartmann Chair in the Electrical and Computer Engineering department.

Jenifer Gómez-Pastora obtained a B.Sc. and M.Sc. in Chemical Engineering and a B.Sc. in Industrial Engineering at the University of Cantabria (Spain). In 2018, she obtained her doctorate in Chemical Engineering at the same university. Afterward, she worked as a postdoctoral researcher in the Department of Chemical and Biomolecular Engineering at Ohio State University (USA). Since 2022, she is an Assistant Professor of Chemical Engineering at Texas Tech University (USA). Her current research activities include the development of cutting-edge magnetic technologies for several biomedical and biological applications, ranging from sensing to diagnosis and treatment.

Kai Wu obtained his Bachelor's degree in Electrical Engineering in 2013 from Northwestern Polytechnical University (China). He further pursued his Ph.D. degree in Electrical Engineering at the University of Minnesota (USA), completing it in 2017. From 2017 to 2020, he served as a postdoctoral fellow at the University of Minnesota, followed by a role as a Researcher 5 from 2020 to 2022. Presently, he holds the position of Assistant Professor at Texas Tech University. His research focuses on various areas including machine learning-assisted healthcare, neuromorphic computing, magnetic biosensors, magnetic nanomaterials, and magnetic particle imaging (MPI).